Christian Hartler, BSc

Water Adsorption on an Iron-Chromium Alloy Surface

MASTER THESIS

For obtaining the academic degree
Diplom-Ingenieur

Master Programme of
Technical Physics

Graz University of Technology

Graz University of Technology

Supervisor:

Univ.-Prof. Dipl.-Ing. Dr.techn. Adolf Winkler

Institute of Solid State Physics

Graz, December 2013

Acknowledgement

This work was a cooperation between the Graz University of Technology and the Optoelectronics Research Center (ORC) in Tampere, which is part of the Tampere University of Technology (TUT). I want to thank professor Adolf Winkler from the Graz University of Technology, who encouraged and guided me through the writing process. He showed me the important parts in a thesis and taught me the needed physical background to complete my work. My thanks goes also to professor Mika Valden and Dr Marko Ahonen from TUT. Prof. Valden made this project possible and came up with the idea of generating a molecular water beam by enhancing a molecular beam surface scattering system. He took care of the administrative steps necessary for me to get a place in his research group as well. Dr Marko Ahonen showed me the surface sensitive techniques and the ultrahigh vacuum system, which are used in the laboratory in TUT. He was very patient with me, gave me confidence in handling ultrahigh vacuum (UHV) systems and even supported me in the writing process, though I already had to leave for Austria because my contract with ORC expired.

Christian Hartler
Graz, December 13, 2013

Abstract

The effects of water adsorption on a Fe-17Cr(100) surface were studied, using molecular beam surface scattering (MBSS) at different surface temperatures. The sample was cleaned in-situ by Ar-Ion sputtering. Afterwards, it was annealed at two different temperatures 900 K and 970 K. Further investigation methods upon adsorption of water included Auger electron spectroscopy (AES), low energy electron diffraction (LEED) and thermal desorption spectroscopy (TDS).

The necessary steps for enhancing our MBSS system were the production and characterization of molecular water beams. The enhancement included building up a water reservoir as source material for the adiabatic gas expansion as well as making the whole system heatable for evaporation of water and elimination of condensation on the pipeline walls. The water gas was seeded with He for higher kinetic energies. The whole setup had to be calibrated to guarantee the correct seeding ratio and the stability of the beam for adsorption experiments.

The adsorption experiments revealed a precursor mediated adsorption process for water and a similar initial sticking coefficient for the two different annealing temperatures at two different surface temperatures. Upon annealing LEED experiments recorded a formed superstructure on the surface of Fe-17Cr(100), which was caused either from water as residual gas or oxygen segregation from the bulk. Since Auger electrons stimulate the desorption of water molecules, the exact determination of the formed superstructure and the chemical composition was not possible. The TD spectra indicated the dissociation of water and a higher bonding energy at elevated surface temperatures by missing desorption peaks for a surface temperature of 323 K during adsorption experiments.

Deutsche Fassung:
Beschluss der Curricula-Kommission für Bachelor-, Master- und Diplomstudien vom 10.11.2008
Genehmigung des Senates am 1.12.2008

EIDESSTATTLICHE ERKLÄRUNG

Ich erkläre an Eides statt, dass ich die vorliegende Arbeit selbstständig verfasst, andere als die angegebenen Quellen/Hilfsmittel nicht benutzt, und die den benutzten Quellen wörtlich und inhaltlich entnommenen Stellen als solche kenntlich gemacht habe.

Graz, am …………………………… ………………………………………………..
(Unterschrift)

Englische Fassung:

STATUTORY DECLARATION

I declare that I have authored this thesis independently, that I have not used other than the declared sources / resources, and that I have explicitly marked all material which has been quoted either literally or by content from the used sources.

…………………………… ………………………………………………..
date (signature)

Contents

Abbreviations and Symbols

a	Atomic distance
AES	Auger Electron Spectroscopy
Ar	Argon
a.u.	Arbitrary units
bcc	Body centered cubic
β	Heating rate
d	Diameter
C	Carbon
Chap.	Chapter
cps	Counts per second
Cr	Chromium
E	Energy
E_a	Adsorption energy
E_d	Desorption energy
E_{pot}	Potential energy
E_T	Translational energy
Eq.	Equation

ϵ_r	Permittivity
F	Flux of the beam
fcc	Face centered cubic
Fe	Iron
Fig.	Figure
γ	Nozzle parameter
h	Planck's constant
H	Hydrogen
H_2O	Water
He	Helium
I	Intensity
J	Nucleation rate
K_{ch}	Characteristic scaling parameter
k_B	Boltzmann's constant
Kn	Knudsen number
λ	Wavelength and in certain cases mean free path
LEED	Low Energy Electron Diffraction
m	Mass
MBSS	Molecular Beam Surface Scattering
MCA	Multi Channel Analyzer
N	Nitrogen
N_A	Avogadro constant

$< n >$	Mean cluster size
ν	Frequency factor
O	Oxygen
OH	Oxyhydroxide
ORC	Optoelectronics Research Center
p	Pressure
p.	Pages
PES	Potential energy hypersurface
Φ	Work function
q_e	Electrical charge
QMS	Quadrupole Mass Spectrometer
R	Universal gas constant
r	Peak to peak ratio
r_{ch}	Characteristic radius
RFA	Retarding Field Analyzer
S	Sticking coefficient
S_0	Initial sticking coefficient
S_Q	Quality of the molecular beam
σ_0	Atom density
σ	Condensation coefficient
T	Temperature
t	Time

t_{meas}	Measured time
t_{QMS}	Detector delay of the QMS
t_{real}	Real flight time
t_{trig}	Trigger delay
T_A	Annealing temperature of the sample
T_{ch}	Characteristic temperature
T_N	Nozzle temperature
T_S	Surface temperature of the sample
T_{term}	Terminal temperature
Tab.	Table
TDS	Thermal Desorption Spectroscopy
Θ	Coverage
θ	Diffraction angle
TPD	Thermal Programmed Desorption
T_S	Surface temperature of the used sample
TUT	Tampere University of Technology
v	Velocity
W	Molar mass
x_{H_2O}	Percentage of water
XPS	X-ray Photoelectron Spectroscopy

1 Introduction

Current applications in construction, car industry and even biomedical engineering utilize stainless steel (FeCr-based alloys) in their field. The reason behind this is their excellent properties and rather cheap production costs. Especially enhancing and adjusting their properties in the near surface region is the goal of current studies. The adjustment of their properties is done by changing small portions in the chemical composition in the near surface region, which influences corrosion resistance, catalysis or biofunctionality. The most important chemical process is the formation of Cr-O layers and its main responsibility is to prevent the effects of corrosion [1, p.171-187]. Another important chemical adsorbent is water. Fundamental interaction between water and solid surfaces can be reviewed by the experimental work of M.A. Henderson [2].

The functional properties invoked by water and oxygen are caused by modifications of the stainless steel surface in the atomic- or nanometer scale. These modifications involve heat treatments and coating techniques. Surface sensitive research methods study the fundamental processes. These studies demand for ultrahigh vacuum (UHV) conditions to exclude interfering materials and processes during the in-situ preparations and measurements. One of these studies dealt with the coadsorption of water and oxygen on stainless steel, which was conducted by D. A. Harrington et al [3]. It concluded that oxygen adsorption was favored over water. Such studies motivated further investigations by the Tampere University of Technology (TUT) [4], [5], [6], [7]. The work of P. Jussila et al [4] had shown that stainless steel exposed to water forms a chromium oxyhydroxide, which reduces the oxidation rate when adsorbed prior to oxygen.

In this work, a molecular water beam was created by enhancing a molecular beam surface scattering (MBSS) system. Utilizing this technique results in a very precise adsorption procedure, which allows to observe the sticking behavior in real time. For investigation a single crystal ferritic stainless steel sample (Fe-17Cr), which surface was prepared along the (100) plane, was used as substrate material. The sample was cleaned in-situ by Ar-Ion sputtering. Afterwards, it was annealed either to 900 K or 970 K. The adsorption process was carried out for the sample temperatures 200 K, 323 K, 400 K, 523 K and 600 K. Upon adsorption the arrangement of water, chemical composition of the surface and the desorption energies were evaluated.

First, the properties of the used materials and the surface sensitive investigation methods will be covered. Then our setup and the enhancements on the MBSS system will be explained. Finally, our measurement results will be shown, followed by a summary with a discussion of the outcome as well as necessary improvements and further investigation procedures to proof the found indications.

2 Principles of Investigated Materials and Research Methods

2.1 Stainless Steel

The properties of stainless steel are determined by crystal structure, composition, size, shape and distribution of the different phases. The property change includes hardness, ductility, strength, impact toughness and creep strength. These phases are alloys usually consisting of Fe, C and elements like Cr, Mn, Ni, Si and Mo. Fe and C is the most investigated alloy but it's not 'stainless'. Chromium is the most important element that contributes in resisting corrosion. Usually, chromiumoxide layers can be formed on the surface to prevent surface corrosion and blocking existing corrosion to spread into the bulk. Heat treatments of these alloys result in different crystal structures and classify the steel type. The phase diagram in figure 2.1 for simple Fe and C show the different phases for certain concentration ratios and temperatures [8, p.91-118].

From the phase diagram all but one of the most important structures, that normal steel forms, can be observed: ferrite, austenite and cementite. Martensitic steel can be obtained by heating up the steel to the austenitic phase, which has a face centered cubic (fcc) lattice, and rapidly cooling it down. This process is called quenching and will trap the carbon atoms, which otherwise would have enough time to diffuse out of the material. This also gives the unique crystal structure to martensite. Local shuffling forms a body centered cubic (bcc) lattice inside of two fcc lattices. Therefore, martensite is a non equilibrium phase and cannot be found in the phase diagram. The most common ferritic stainless steel is α-ferrite. It has a bcc structure and the carbon atoms are randomly distributed. This distribution is due to the low solubility of carbon atoms in the ferritic phase [9, chap2],[10, chap.2],[8, p.695-735].

The 2-dimensional crystal structure at the surface is characterized by the angle of the cutting plane. Examples for fcc and bcc structures are given in figure 2.2 and 2.3, which are fundamental for surface investigation. The indicator for the reactivity of the surface is the surface atom density, which influences the work function. The surface atom density can be calculated by the Miller indices hkl

$$\sigma_0 = \frac{1}{A_{hkl}} = \frac{4}{Qa^2(h^2+k^2+l^2)^{1/2}} \tag{2.1}$$

for fcc and bcc lattices. A_{hkl} is the area of the surface unit cell, a the lattice constant in the bulk and Q can be obtained by the following rules [11, p.10-14]:

bcc: $Q = 2$ if (h+k+l) is even, $Q = 4$ if (h+k+l) is odd
fcc: $Q = 1$ if h, k and l are all odd, otherwise $Q = 2$

Since this is the ideal case, the reactivity of the surface can be influenced additionally by surface defects. These defects can be a combination of adatoms, vacancies, steps or terraces [10, chap.2].

Corrosion is one of the reactions that can occur due to the reactivity of the surface. As for stainless steel materials, it can appear under different circumstances because these materials are only corrosion resistant and not absolutely stainless. As mentioned before, chromium shows a great resistance against corrosion at higher concentration once it is above 10 %. But the obtained resistance is only good in the neutral and acidic pH ranges and is little effective in high-pH environments. Other materials like molybdenum help to increase the resistance. On the other hand adding carbon, which is important for hardening the steel, to the alloy makes the steel vulnerable to localized corrosion attacks. The reason is that carbon reacts with chromium causing a decrease in the localized pure chromium concentration.

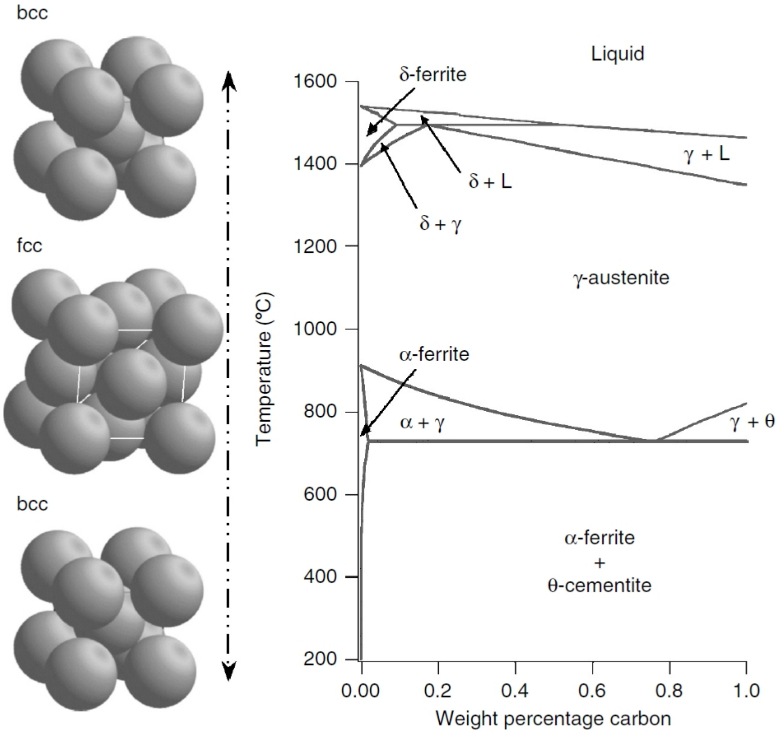

Figure 2.1: Phase diagram of Fe-C alloy. The phases can be categorized into austenite, ferrite, cementite and liquid [8, p.93].

Therefore, the chemical composition has to be matched for certain applications [9, chap.2].

The environment plays a mayor role for the appearance of corrosion. Typical atmospheric conditions mean that the steel is exposed to natural elements in the air at ambient temperature. The atmosphere consists mainly of water, carbondioxide, oxygen and other more aggressive pollutants that have a great catalytic effect in generating corrosion. Especially in cities and marine environments the air is contaminated with sulfur and chlorides. If catalytic effects would be excluded and only deionized water would be considered, the stainless steel should be free from any localized corrosion effects. Deionized water usually contains low concentration of dissolved salts and some dissolved carbon dioxides from the air. In the case of normal fresh water the situation is different. Additionally, it consists of some chlorides. To prevent stainless steel from reactions with chloride, which

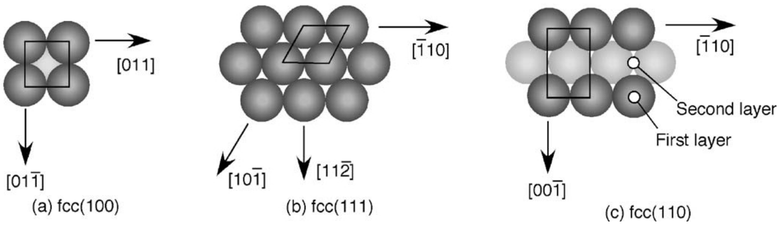

(a) fcc(100)
(b) fcc(111)
(c) fcc(110)

Figure 2.2: Crystal structures at the surface of the face centered cubic (fcc) low index planes: (a) fcc(100), (b) fcc(111) and (c) fcc(110) [11, p.10].

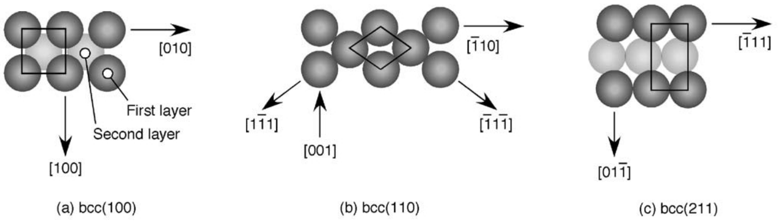

(a) bcc(100)
(b) bcc(110)
(c) bcc(211)

Figure 2.3: Crystal structures at the surface of the body centered cubic (bcc) low index planes: (a) bcc(100), (b) bcc(110) and (c) bcc(211) [11, p.11].

would lead to corrosion, the alloying with corrosion resistant materials, especially molybdenum, must increase. Hence, reactive elements, that support solution conductivity, are important for establishing corrosion. Furthermore, heating up the environment assists chemical reactions and further raise the chances of corrosion [9, chap.1-2].

2.2 Water

Water is formed by a covalent bond of 2 hydrogen atoms with an oxygen atom (Fig. 2.4). The distance between the O-H bonding is about 0.96 Å and the H-O-H angle is about 104.5°. The bond angle also describes the nuclear geometry of water, which results in a puckered hexagonal and pentagonal ring structures in condensed phases. The most common interaction between the water molecules is through hydrogen bonds [12, p.29-31].

2.2.1 Hydrogen Bond

Hydrogen bonds (H-bonds) result from an attractive interaction between the electron donor, which is hydrogen, and the electron acceptor, which in case of water is oxygen. Oxygen is electronegative and therefore an electron draws closer from one hydrogen atom to oxygen. Hydrogen then is partially positively and oxygen partially negatively charged. This is due to the nonlinearity of the water molecule that produces a polar molecule with an electrical dipole moment. The same procedure happens in another water molecule. The consequence is that the partially positively charged hydrogen will attract the partially negatively charged oxygen from the other molecule. Therefore, an electrostatic interaction between those two molecules will occur and form a "hydrogen bridge".

$$H - O^{\delta-} - H^{\delta+} \cdots O^{\delta-} - 2H^{\delta+}$$

H-bonding has the side effect that it pulls the H atom away from the covalently bonded O atom. This can be seen in a substantial red shift from the stretching of vibrational frequencies. In general H-bonds can be classified into three types depending on the interaction strength of the bond. Therefore it can be divided into strong, moderate and weak H-bonds [13, p.2-4]. The classification according to bond strength, angle and red shift can be looked up in table 2.1.

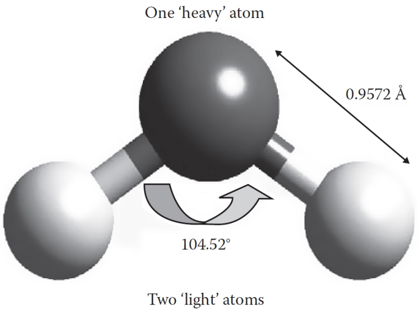

Figure 2.4: Schematic representation of the water molecule.[12, p.31]

The directionality of the bonds comes from the length and the angle of the bond, which defines also the strength of the bond. Especially the length of the bond is

Table 2.1: Classification of the three major types of H-bonds and their characteristics. Water has a bonding length of 1.9 Å and a bonding energy of $1.4 * 10^{23}$ eV/mol or about 5 kcal/mol. This means water is a moderate H-bond. [13, p.3]

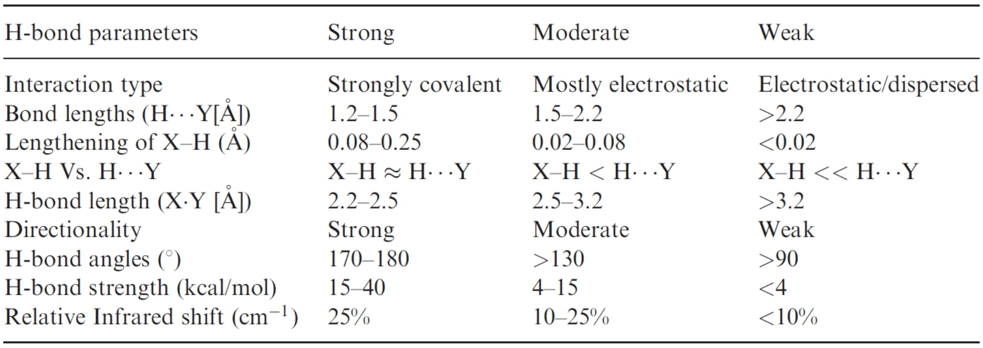

H-bond parameters	Strong	Moderate	Weak
Interaction type	Strongly covalent	Mostly electrostatic	Electrostatic/dispersed
Bond lengths ($H \cdots Y$[Å])	1.2–1.5	1.5–2.2	>2.2
Lengthening of X–H (Å)	0.08–0.25	0.02–0.08	<0.02
X–H Vs. $H \cdots Y$	$X–H \approx H \cdots Y$	$X–H < H \cdots Y$	$X–H << H \cdots Y$
H-bond length (X·Y [Å])	2.2–2.5	2.5–3.2	>3.2
Directionality	Strong	Moderate	Weak
H-bond angles (°)	170–180	>130	>90
H-bond strength (kcal/mol)	15–40	4–15	<4
Relative Infrared shift (cm^{-1})	25%	10–25%	<10%

very important since the strength decreases exponentially with the distance. The interaction strength for water is about $1.4 * 10^{23}$ eV/mol (at 0 °C) and the typical bond length is about 1.9 Å. This means water can be classified as a moderate H-bond, which is the most common group. Therefore H-bond of water is mostly determined by electrostatic forces (approximately 90 %) and also partly by some covalent forces (approximately 10 %). But the interaction is not that simple since van der Waals forces and polarization of the molecules contribute to the bonding. The H-bond is the driving force for water clusters to form tetrahedral structures. For other ordinary fluids on the other hand the structure is different because ordinary fluids have 12 nearest neighbors whereas water only has four. The tetrahedral network is a result of the preferred linear bonding with a contact angle of about 180° over nonlinear bonding (contact angle about $180 \pm 20°$). In solid ice this tetrahedral symmetry is long ranged and permanent, but it's fluctuating in water (the bonding lasts only for about 1 picosecond) and short ranged. If the liquid is heated up, the bonding becomes weaker. Due to the strength of H-bonds, the energy input required for evaporating water is higher compared to other substances because the H-bonds have to be broken [12, p.69-72],[13, p.2-4]. Those considerations have to be taken into account for producing a supersonic molecular water beam, which will be described further in chapter 2.3.3.

2.3 Surface Science Approach

The surface science approach was used in this thesis to understand the initial oxidation stages and OH-bondings of stainless steel. Especially, Gerhard Ertl had a great influence in this field, who won the Nobel Prize in Chemistry ”for his studies of chemical processes on solid surfaces” in 2007 [14]. Since surface science approaches probe interfaces at a molecular level, it has to utilize vacuum conditions. Vacuum conditions will ensure that the interface is well-characterized. This makes predictions of the investigated reaction possible. Also the investigation techniques require vacuum conditions to function. For example techniques like low energy electron diffraction utilizes electron beams. If atmospheric conditions are present, the electrons of the beam would scatter at the gas molecules in the chamber before they actually reach the surface of the sample. Low electron energy diffraction and some other surface analyzing techniques: molecular beam surface scattering, Auger electron spectroscopy and thermal desorption spectroscopy will be explained in this chapter.

2.3.1 Interactions of Molecules with the Surface

Interaction of molecules with surfaces includes various processes like adsorption, dissociation during adsorption, segregation into the bulk and desorption. If a molecule is brought closer to the surface it experiences forces. The most important ones are the Van der Waals force, the electrostatic force and steric force. The Coulomb force is an electrostatic force between two charges. Given two electrical charges $q_{e,1}$ and $q_{e,2}$ the electrostatic potential energy decreases with the distance r:

$$E_{pot} = \frac{q_{e,1} q_{e,2}}{4\pi\epsilon_r r} \tag{2.2}$$

with ϵ_r the permittivity. Furthermore, the electrostatic force decreases from charged to polarized particles. Therefore, charge-charge interactions have a higher potential energy than dipole-dipole interactions. Since atoms need to occupy a certain amount of space steric forces arise to counteract electrostatic forces. This can be explained by the Pauli exclusion principle because not every quantum number of two electrons must be the same. The Van der Waals force usually occurs in nonpolar elements and is a weak force between them. It can be divided into Keesom force (interaction between two permanent dipoles), Debye force (interaction between a permanent dipole and an induced dipole) and the London dispersion force (interactions between two induced dipoles). The electrostatic forces describe the chemisorption of molecules on the surface, whereas the Van der Waals force is responsible for physisorption [15, p.80-84].

The sum of those potentials is called the multidimensional potential energy hypersurface (PES). The shape of the PES can result in three different adsorption behavior, non-activated adsorption, activated adsorption and precursor-state mediated adsorption (Fig. 2.5). The difference between these types of adsorption can be determined by the sticking coefficient for different kinetic energies and coverages of the adsorbate. This allows to obtain information on the kinetics and dynamics of adsorption [11, p.133-144].

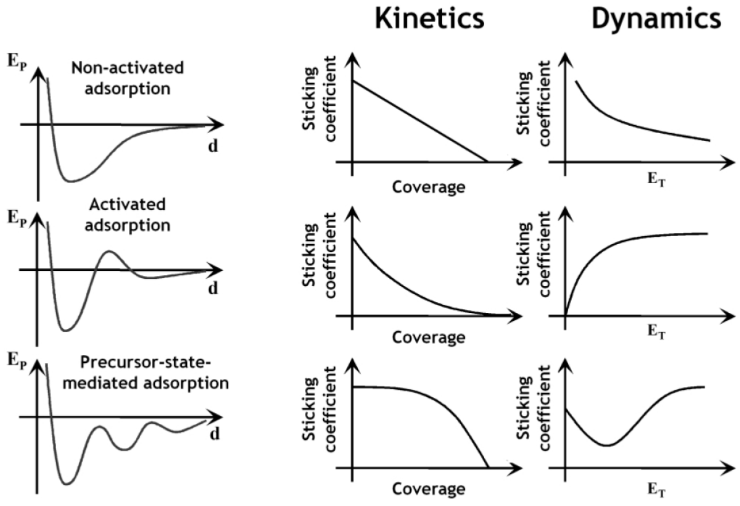

Figure 2.5: Scheme of the dynamics and kinetics of adsorption for the three basic adsorption scenarios: first row non-activated adsorption, second row activated adsorption and last row precursor-state mediated adsorption [16].

The bonding of the molecule can have a strong influence on the adsorption process.

When two atoms form a molecule their atomic orbitals (AO) define the molecular orbital (MO). The MO has a bonding and an antibonding state with an energy shift to the mean energies of the AO. Depending on the interactions first the bonding then the antibonding state is filled by the electrons. In general, the antibonding state is more repulsive than the attraction from the bonding state. This means when the antibonding state is filled the molecule dissociates into its parts. The energy state of the surface on the other hand is broadened, since a lot of particles form the surface, which therefore is a combination of all orbitals. If a stable molecule starts to adsorb on the surface, there will be an additional energy shift due to the bonding or antibonding of the molecule to the surface. Moreover, these bonding and antibonding states are broadened (Fig. 2.6). Depending on the interactions with the surface, the antibonding state of the molecules can be filled before the antibonding state between the surface and atoms is filled. This leads to dissociation of the molecule and enables additional possibilities for reactions on the surface between different molecules, which is the cornerstones in catalysis [11, p.121-133],[17, p.75-83].

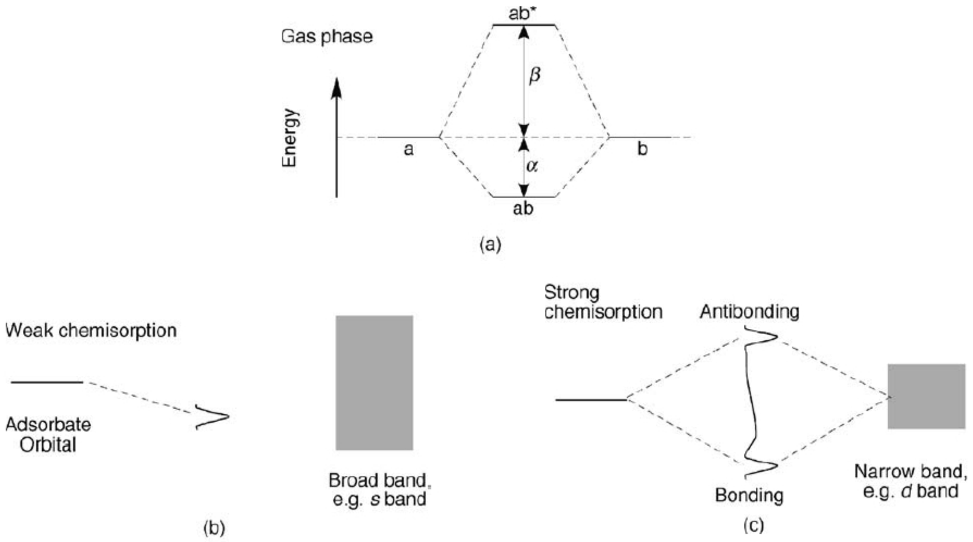

Figure 2.6: Orbital ineraction (a) between two atoms, (b) of weak chemisorption of an atom on a surface, (c) strong chemisorption of an atom on a surface [11, p.122].

An important effect that has to be taken into account during adsorption of a molecule is that the sticking coefficient will change due to the coverage. The simplest case to describe this behavior is the Langmuir adsorption model. It makes the assumption that the limiting factor for adsorption is the coverage, all adsorption sites adsorb equally strong and those sites can be occupied by one molecule. The sticking coefficient can be described as

$$S = \sigma f(\Theta) exp(-\frac{E_a}{k_B T}) \tag{2.3}$$

with σ the condensation coefficient, E_a the activation energy for adsorption, T the temperature, k_B the Boltzmann constant and $f(\Theta)$ the probability for the molecule to find a free adsorption site, where Θ describes the percentage of surface coverage. In the case that the molecule doesn't dissociate, the probability is given by

$$f(\Theta) = 1 - \Theta \tag{2.4}$$

whereas for dissociative adsorption of a molecule with two atoms the probability is

$$f(\Theta) = (1 - \Theta)^2 \tag{2.5}$$

Therefore, for a molecule consisting of n atoms the probability for dissociative adsorption is

$$f(\Theta) = (1 - \Theta)^n \tag{2.6}$$

because n atoms can occupy n sites on the surface. If the surface has precursor states, which the molecule can occupy, the probability gains an additional dependency:

$$f(\Theta) = \frac{(1 + K)(1 - \Theta)^n}{1 + K(1 - \Theta)^n} \tag{2.7}$$

with $K = k_a/k_d$ a temperature dependent parameter from the precursor that is defined by the desorption rate constant k_d and the adsorption rate constant k_a [18, p.295-301]. The behavior of the sticking coefficient as a function of coverage for different adsorption kinetics can be looked up in figure 2.7.

After the molecule is adsorbed on the surface it might also segregate into the bulk

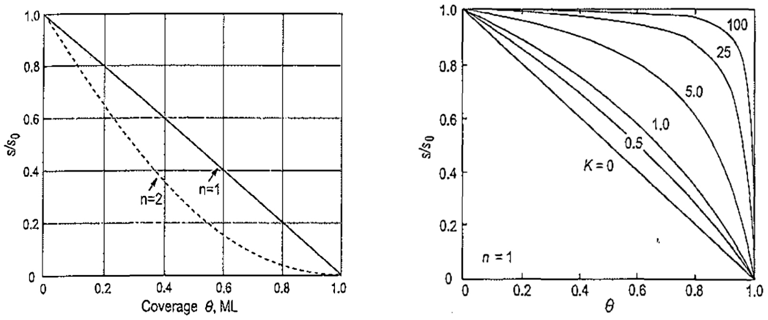

Figure 2.7: Sticking coefficient dependencies on the coverage for Langmuir adsorption model: (Left) non-dissociative (n=1) and dissociative (n=2). (Right) Precursor mediated adsorption for non-dissociative chemisorption, where K is the precursor parameter. [18, p. 297 and 300].

depending on the segregation and mixing energy. The segregation energy describes the dependence of the surface free energy to the coverage of adsorbates. If the surface free energy is increased by the amount of adsorbed molecules, it results in the segregation of the adsorbates since an increase of energy is unfavorable (segregation energy is positive). On the other hand if the surface free energy is decreased by the adsorbates, the adsorbates will stay at the surface (segregation energy is negative). The mixing energy on the other hand describes aggregation (negative) and dissolution (positive) of the adsorbates, which results from an energy gain of forming a bond between different kinds of atoms. This leads to four different situations that can occur, which are shown in figure 2.8. [19, p.211-213]

2.3.2 Vacuum and Preparation of the Sample

A true vacuum is a space that is empty of matter, but there is no such location on Earth, and not even in outer space. This means that vacuum has to be produced by pumping out a chamber. The pressure in the chamber at the end of the pumping procedure defines the quality of the vacuum (Tab.2.2). The needed pressure p can be determined by considering different conditions, which have to be fulfilled. The first consideration to make is that the sample surface has to be clean of residual gas. This leaves two questions, how many molecules will strike the surface in a

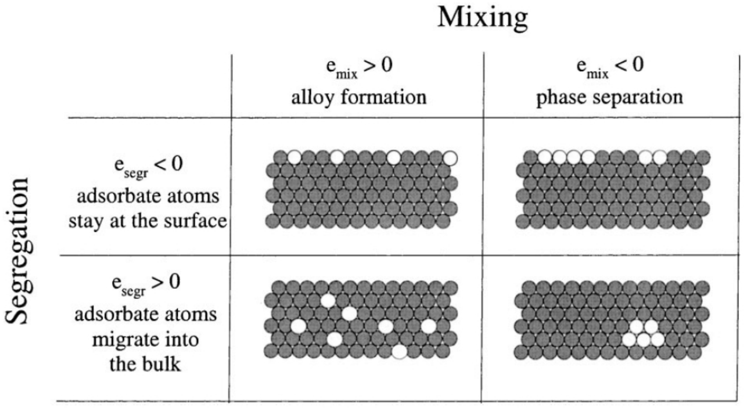

Figure 2.8: Scheme of four different adsorbate behaviors due to segregation and mixing energy. The adsorbate is marked with white circles and the substrate with grey circles [19, p.212].

given time and how long it will take till a monolayer of residual gas will be formed on the surface. The expression that describes the number of gas molecules that strikes the surface at a given time is the impingement rate. It is defined as

Table 2.2: Classification of vacuum according to common pressure values [18, p.20].
p ... pressure of environment
n ... molecular density
I ... impingement rate
λ ... mean free path
τ ... monolayer formation time

	$p\,[Torr]$	$n\,[cm^{-3}]$	$I\,[cm^{-2}s^{-1}]$	$\lambda\,[m]$	$\tau\,[s]$
Atmospheric pressure	760	$2 * 10^{19}$	$3 * 10^{23}$	$70 * 10^{-9}$	$3 * 10^{-9}$
Low vacuum	1	$3 * 10^{16}$	$4 * 10^{20}$	$50 * 10^{-6}$	$2 * 10^{-6}$
Medium vacuum	10^{-3}	$3 * 10^{13}$	$4 * 10^{17}$	$50 * 10^{-3}$	$2 * 10^{-3}$
High vacuum	10^{-6}	$3 * 10^{10}$	$4 * 10^{14}$	50	2
Ultra high vacuum	10^{-9}	$3 * 10^{7}$	$4 * 10^{11}$	$50 * 10^{3}$	3600

$$I = \frac{p}{\sqrt{2\pi m k_B T}} \tag{2.8}$$

with m the mass of the impinging gas, k_B Boltzmann constant and T the temperature. The impingement rate also influences the time for forming a monolayer of residual gas on the surface. This leads to the expression for the monolayer formation time

$$\tau = \frac{n_0}{I} = \frac{n_0\sqrt{2\pi m k_B T}}{p} \tag{2.9}$$

with n_0 the monolayer density. This means in the case of room temperature, which is about 300 K and atmospheric pressure of $p = 760\,\mathrm{Torr}$ the impingement rate would be like $I = 3 * 10^{23}\,\mathrm{molecules/cm^2s}$ and the time to form a monolayer is $\tau = 3\,\mathrm{ns}$. In the case of ultrahigh vacuum with a pressure of $p = 10^{-10}\,\mathrm{Torr}$ the impingement rate and the time to form a monolayer reduces to $I = 4 * 10^{10}\,\mathrm{molecules/cm^2s}$ and $\tau = 10\,\mathrm{hours}$. When dealing with an analyzing technique that involves electron beams, the following considerations have to be taken into account. The mean free path, which is the average length a particle can travel before colliding with another particle, is important for using such a technique:

$$\lambda = \frac{k_B T}{\sqrt{2}\sigma p} \tag{2.10}$$

with k_B the Boltzmann constant, T the temperature, σ the collision cross section of the particle and p the pressure inside the chamber. The collision cross section of N_2 molecules is $\sigma = 0.43\,\mathrm{nm^2}$. If atmospheric conditions are present then the mean free path would be only 70 nm, which is definitely not enough to perform surface analysis. On the other hand if ultra high vacuum conditions of $p = 10^{-10}\,\mathrm{Torr}$ are present, the mean free path increases over 500 km. Theoretically for utilizing electron spectroscopy a mean free path should be greater than 1 m, but longer distances are required to reduce the noise of the detector [18, p.19-20],[11, p.51-53], [20, p.10-11].

Therefore, ultrahigh vacuum conditions are typical for most surface analyzing techniques. To maintain those conditions, special vacuum pumps like turbopumps are a necessity. The flux of molecules a vacuum pump can remove, which is called the throughput Q_t, is defined as

$$Q_t = S p_{eq} \tag{2.11}$$

with $S = \frac{dV}{dt}$ the pumping speed, which is the effective mean volume flow of a vacuum pump at the inlet port, and p the equilibrium pressure. The effective pumping speed S_{eff} can be calculated by the conductance C of the inlet port and the pumping speed S of the attached vacuum pump:

$$\frac{1}{S_{eff}} = \frac{1}{S} + \frac{1}{C} \tag{2.12}$$

In case of changing pressure, the so called “pumping equation” is as follows:

$$Sp(t) = Q_i - V\frac{dp}{dt} \tag{2.13}$$

with $-V\frac{dp}{dt}$ the decreasing number of molecules in the gas phase and Q_i the gas flux coming from degassing of chamber walls, as well as real and virtual leaks. After integrating this equation and considering Q_i constant, the pressure after a certain pumping time inside the chamber can be obtained

$$p(t) = p_{end} + (p_0 - p_{end})e^{-S\frac{t}{V}} \tag{2.14}$$

with p_0 the initial pressure and p_{end} the final pressure when the leaks and degassing chamber walls are in equilibrium with the pumping. Additionally, out-baking the vacuum chamber supports the degassing of the chamber walls and evaporating condensed water, which otherwise would be slowly pumped off the walls. This measurement makes it possible to reach the final pressure much faster and gets rid of the condensed water [18, p.20-22].

The previously obtained equations give information on the choice of the used materials of the chamber walls, planning the structure of the chamber like the inlet port and choosing the right vacuum pumps. This means in case of choosing the right materials, only low degassing, nonporous and temperature stable materials like stainless steel, copper, ceramics or glass should be used as chamber walls. The pumping system for a vacuum chamber consists of a forepump and a molecular pump. The forepump is necessary to reach a low enough pressure so that the molecular pump can function. The most common forepump is the rotary vane pump. Inside of the vane pump there is a cavity with a vane mounted to a rotor. The vanes make contact with the walls and are covered with oil to reduce the leakage. The rotation will drag the gas. As for the molecular pumps there is the oil diffusion pump and the turbomolecular pump that are most important. In an oil diffusion pump, oil is evaporated and directed through a jet assembly to trap gas molecules. The jet hits the cold chamber walls and the oil with the trapped gas go to the bottom, where they are heated up. The oil then is used for the jet again, whereas the gas is collected at the bottom where it can be easily pumped away by the forepump. The turbomolecular pump on the other hand utilizes rotating and static blades to get rid of the gas. It has a high rotation speed, which is necessary to give the gas molecules a momentum into the direction of the exhaust. For the creation of even better vacuum conditions pumps that trap the molecules at the chamber walls are necessary. The typical pump for this measure would be the ion pump, that utilizes a magnetic field in a cathode/anode arrangement to ionize the gas molecules, which then will be accelerated towards the cathode. The cathode material will sputter from the impact. Both the gas molecules and the cathode material fly towards the chamber walls. There, the cathode material binds the gas molecules onto the chamber walls by chemisorption.

When the pressure inside the vacuum chamber drops below 10^{-3} Torr, it's determined typically by an ionization gauge. The ion gauge has a cathode/anode arrangement. Electrons will be ejected from the cathode and accelerated towards the anode. On their way, they will collide with gas molecules, which will be ionized. The ionized gas molecules will be attracted towards a grounded collector at the center of the gauge. The current measured at the collector is directly dependent on the gas pressure due to the ionized gas molecules [18, p.24-35].

The cleaning of the sample surface can be divided into two steps, ex-situ and in-situ. Ex-situ preparation involves mechanical and chemical cleaning before introducing the sample into the vacuum chamber. Polishing the sample, using ethanol for removing residual oil and putting the sample in an ultrasonic cleaner are typical ex-situ methods. In-situ preparations is done when UHV-conditions are present and before the experiment starts. The most common techniques are cleavage, heating, chemical processing and ion sputtering (Fig. 2.9). In the case of cleavage the sample material has notches cut into it. A wedge, that can be controlled, is used to cleave away the uppermost layers. Heating is done by annealing the sample either with an applied electrical current, bombarding the surface with electrons or

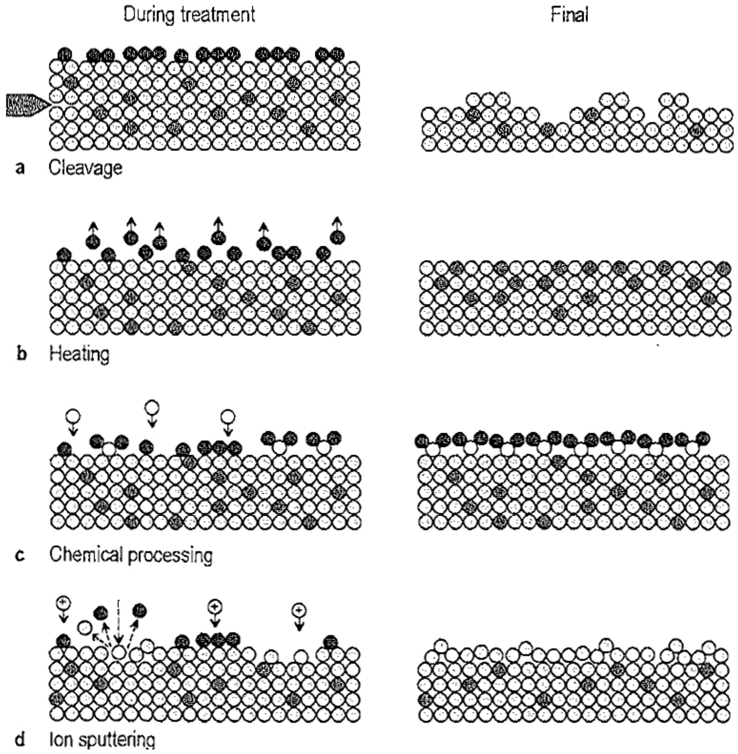

Figure 2.9: Schematics of surface cleaning techniques in-situ: (a) cleavage, (b) heating, (c) chemical processing and (d) ion bombardment. Sample material is represented by light gray circles, foreign species by dark gray circles and impurities by black circles [18, p.36].

anneal it with a laser. This will cause the desorption of weakly bonded impurities. Chemical processing utilizes reactive gases, which form weak-bonded compounds of strong-bonded impurities. To get rid of those compounds the sample is heated up and the compounds will simply desorb from the surface. Ion sputtering bombards the surface with a beam of noble gas ions like Ar^+. The beam is produced by injecting noble gas directly into the ion gun or into the UHV-chamber. The gas flow is regulated by a leak valve. Inside the gun noble gas ions are produced by electrons from a cathode/anode arrangement. After the ionizer part, they are accelerated towards the sample surface up to the desired kinetic energy. The sample should be annealed after the sputtering process due to the degradation of the surface structure. The annealing process will remove embedded and adsorbed ions to restore the crystallography of the surface [18, p.35-39].

2.3.3 Molecular Beam Surface Scattering

Molecular beam surface scattering (MBSS) is a technique to experimentally obtain the adsorption kinetics and dynamics of surfaces. This technique utilizes a molecular beam, which is directed to a sample. The molecules will adsorb on the surface of the sample if certain conditions are met and otherwise scatter away. After some time the surface of the sample will be saturated and every incoming molecule will scatter away. The molecules that are scattered will be detected by a quadrupole mass spectrometer (QMS). The QMS filters ions based on their mass-to-charge ratio by applying an oscillating electric field to four parallel rods. The measured ”sticking” signal has to be compared with a reference signal, which can be obtained by making the same experiment with the non reactive part of the sample holder. This procedure is called “The direct reflectivity method of King and Wells” [21].

The comparison makes it possible to determine the sticking coefficient at different coverages of the surface. First of all, it is necessary to determine the time dependence of the sticking coefficient

$$S(t) = \frac{I_0(t) - I(t)}{I_0(t)} \tag{2.15}$$

and then the coverage during the experiment can be determined

$$\Theta(t) = F \int_0^t S(\tau) d\tau \tag{2.16}$$

with I_0 the intensity of the reference signal, I the intensity of the sticking signal, F the flux of the molecular beam and t the time. The dependency of the sticking coefficient to the coverage of the surface describes the kinetics of the adsorption. If the translational energy of the beam is varied, the sticking probability of the experiment will also change. This results in a dependency of the sticking probability on the translational energy of the beam, which gives information on the dynamics of the adsorption. With the measurement of the adsorption dynamics, the activation energy of the adsorption can be calculated, and in principle information on the whole potential energy surface can be gained [16, p.18-22].

Molecular Beams

There are two types of molecular beams, the effusive Knudsen and the supersonic beam. The basic principle is that a chamber is pressurized with gas. This gas can expand isentropically into the expansion chamber through a tiny orifice. In the case of the Knudsen beam the pressure difference between the expansion chamber and the gas chamber is low and therefore leads to an effusive beam, whereas in the case of the supersonic beam this difference is high and should be at the minimum order of $10^3 - 10^4$. The high pressure difference allows the molecules to get accelerated up to “supersonic” velocities. The “supersonic” speed is only due to the low speed of sound a, which is defined as:

$$a = \sqrt{\frac{\gamma T}{k_B}} \tag{2.17}$$

with γ the ratio of heat capacities at constant pressure and T the temperature of the gas. Due to the expansion the temperature of the gas molecules will become very low, which results in a low speed of sound. Furthermore, the molecules are going to experience a high collision rate with each other directly after exiting the chamber which leads to the narrow speed distribution of the beam as well as to some other important characteristics. This happens as follows. The faster molecules will speed up the slower molecules while the slower ones slow down the faster molecules resulting in reducing the spread in velocity. Collisions in the transverse directions of the beam let molecules either get scattered out of the beam or transfer their transverse kinetic energy into kinetic energy parallel alongside the beam so the beam gets focused. The collisions affect the vibrational (only with a low wavenumber) and rotational energies of the beam. This leads to the equilibrium of their energies by transferring their energies to the translational energy. In comparison with the kinetic energy, which only take a few collisions to equilibrate, the rotational energies take tens to hundreds of collisions to reach the equilibrium state. The expansion of the beam from the gas chamber into the expansion chamber has the effect to cool these energies down. This is so effective that temperatures lower than 10 K can be achieved and all degrees of freedom are cooled into stream velocity. However, high wavenumber vibrational energies are almost unaffected by the expansion because they need too many collisions. The molecules in the expansion region usually take about 100-1000 collisions before a molecular beam is formed. In this state the molecules won't collide with each other again before hitting a target. Hence, the supersonic molecular beam has a high translational energy alongside the flow direction with an extreme low rotational and translational temperature, but a nearly unaffected vibrational temperature close to the nozzle temperature. The maximum or terminal velocity of the beam can be expressed as:

$$v = (\frac{2k_B(T_{noz} - T_{term})}{W/N_A} \frac{\gamma}{\gamma - 1})^{1/2} \tag{2.18}$$

with W for the molar weight of the gas in the chamber, N_A the Avogadro constant, γ the ratio of the heat capacities, T_{noz} the temperature of the nozzle and T_{term} the terminal temperature of the beam. If the gas chamber is pressurized with additional gases, then the average of the molar weight W_{avg} has to be calculated. For a gas mixture the translational energy for one component $E_{T,comp}$ can be expressed as:

$$E_{T,comp} = \frac{W_{comp}}{W_{avg}} \frac{\gamma}{\gamma - 1} k_B(T_{noz} - T_{term}) \tag{2.19}$$

with W_{comp} the molar mass of the gas component in the mixture. During the expansion from the nozzle to the vacuum chamber, also shock waves will occur. If these waves aren't stopped, these barrel shocks will return to the molecular beam and decelerate it to subsonic speed. A solution for this problem is to place a skimmer in the zone of silence (Fig. 2.10). This has the advantage to block background gas from entering the beam line [19, p.178-183], [11, p.57-62] [22, p.14-53],[23, chapter 2].

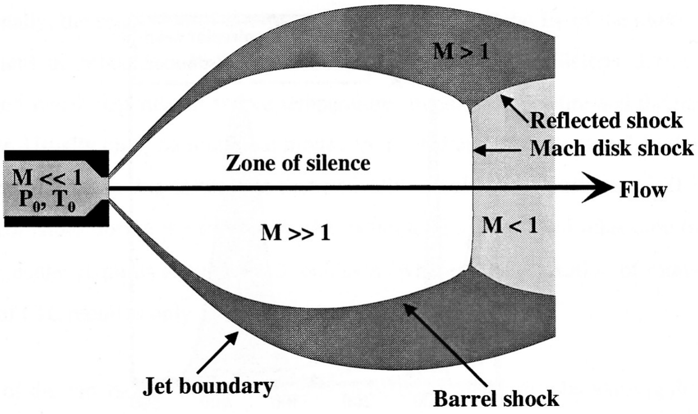

Figure 2.10: Expansion of the pressurized gas from the nozzle into the vacuum chamber. A skimmer has to be placed inside the zone of silence to avoid deceleration of the molecular beam [16, p.11].

Time-of-Flight Measurement

Time-of-flight measurements (TOF) are used to determine the translational energy of the molecular beam. During TOF measurements the flight time of the molecular beam for a certain distance is measured by a QMS. For these measurements it's also necessary to chop the beam into pieces to get a pulsed signal. But since the detector has delays, the measured time must be adjusted to get the real flight time:

$$t_{real} = t_{meas} - t_{trig} - t_{QMS} \tag{2.20}$$

with t_{meas} the measured time of flight, t_{QMS} the delay from the QMS detector and t_{trig} the delay from the trigger. The detector delay is proportional to the square root of the mass-charge ratio:

$$t_{QMS} = K\sqrt{m/q} \tag{2.21}$$

K is a constant that can be determined experimentally in two different ways. In the first one, a noble gas like argon with two different ionization stages is used. This means that if for one experiment single ionized argon and for another experiment double ionized argon were measured, it would result in two different t_{meas}. Since the real flight time and the trigger delay would be the same, t_{QMS} can be obtained. The second way is to perform TOF experiments of two monoatomic gases with different masses. The average translational energy for these gases is $(5/2)k_B T_{noz}$. This leads to the calculation of the real time of flight:

$$t_{real} = \frac{s}{v} = \frac{s}{\sqrt{\frac{2\overline{E}}{m}}} = \frac{s}{\sqrt{\frac{5k_B T_0}{m}}} \tag{2.22}$$

with s the length of the flight path, k_B the Boltzmann constant, T_0 the temperature of the nozzle, v the average velocity, m the mass of the used gas and $\overline{E}$ the average translational energy. Since t_{real} is known, the constant K can be calculated:

$$K = \frac{(t_{A,meas} - t_{A,real}) - (t_{B,meas} - t_{B,real})}{\sqrt{\frac{m_A}{q_A}} - \sqrt{\frac{m_B}{q_B}}} \tag{2.23}$$

where A and B in the index marks the corresponding gas. The second method is used in this thesis to determine the detector delay. To get the trigger delay it's necessary to transform equation 2.20 into:

$$t_{trig} = t_{meas} - t_{real} - K\sqrt{m/q} \tag{2.24}$$

After obtaining the real time of flight and calculating the average velocity of the beam for a known flight distance, the translational energy can be calculated using

$$E_T = \frac{Wv^2}{2N_A} \tag{2.25}$$

with W the molar weight of the molecule, N_A Avogadro's constant and v the average velocity [16, p.14-18],[19, p.181-183]. It should be noticed that the obtained energy is the same as in Eq.2.19.

Furthermore, from TOF measurements a velocity distribution is obtained that can be used to determine the terminal temperature of the beam. The terminal temperature corresponds to a terminal velocity α, which is characterized by

$$\alpha = \sqrt{\frac{2k_B T_{term}}{m}} \tag{2.26}$$

with k_B the Boltzmann constant, T_{term} the terminal temperature and m the mass of the molecule. The speed ratio between the average velocity v and the terminal velocity α describes the quality of the beam:

$$S_Q = \frac{v}{\alpha} \tag{2.27}$$

The speed ratio can also be experimentally determined by the velocity distribution of the TOF measurement:

$$S_Q \approx 2\sqrt{ln2}\frac{v}{\Delta v} \tag{2.28}$$

with Δv the full width at half maximum of the measured velocity speed distribution [24, p.24-26]. The terminal temperature can be calculated by combining the above equations:

$$T_{term} = \frac{m\Delta v^2}{8k_B ln2} \tag{2.29}$$

Cluster Formation

The free jet expansion of an MBSS system usually is used for operating with an unclustered source, which is wanted in most cases to prevent additional parameters. Nevertheless, during the adiabatic expansion in a free jet of an unsaturated gas like vaporized water, the expanding gas most likely will form clusters and nucleate. In nature, usually heterogeneous nucleation occurs, for example forming bubbles when sparkling water is poured into a glass. But the more simple form of nucleation is homogeneous nucleation, which occurs in the absence of an external surface. Therefore, homogeneous nucleation is the probable describing process in the free jet expansion. At the beginning of the process, small clusters are formed. If other molecules condensate, these clusters will grow and finally aggregate to build up large clusters. The most important factor for nucleation is the change in Gibb's free energy. It describes the condensation of the gas molecules at a certain pressure into a drop. The surface tension and especially the vapor pressure of the molecules play crucial roles in defining the critical radius of the drop. If the radius of the drop is smaller than the critical radius the drop is instable and will evaporate again. But if the radius is higher, the drop is stable and it can grow. The classical nucleation theory aims to find the nucleation rate J, where clusters with the critical size are formed. Therefore, it's dependent on the change in Gibb's free energy, which includes the previous considerations:

$$J \propto exp(-\frac{\Delta G}{k_B T}) \tag{2.30}$$

with ΔG the change in Gibb's free energy, k_B the Boltzmann constant, T the temperature [15]. For the free jet expansion the formed cluster size varies from dimer to about 50000 molecules per cluster [25],[22, p.380-410].

The size distribution can be changed by the source parameter, in particular the inlet pressure p, temperature T and the orifice diameter d. Also the use of seeding gas influences the nucleation rate. One way to find out, if classical nucleation theory is applicable on free jet expansions, is by calculating the Knudsen number:

$$Kn = \lambda / d \tag{2.31}$$

with λ the mean free path and d the diameter of the orifice [25, p.48]. It also defines how many collisions will occur during expansion. This means for a high pressure, there are a lot of collisions during gas expansion, until the gas becomes a molecular beam. But for dealing with clusters in an MBSS system the nucleation rate is not as important as the real cluster size. Hagena [26] introduced a scaling law, an empirical formula for calculating the mean cluster size:

$$< n >= D(\frac{\Gamma^*}{1000})^a \tag{2.32}$$

where D and a are fit parameters depending on the gas molecule and Γ^* is a dimensionless parameter, which compares the characteristic scaling parameter K_{ch} for the gas molecule and the nozzle parameter Γ:

$$\Gamma^* = \Gamma / K_{ch} \tag{2.33}$$

The characteristic scaling parameter is described by:

$$K_{ch} = r_{ch}^{q-3} T_{ch}^{\alpha} \tag{2.34}$$

with r_{ch} the characteristic radius, T_{ch} the characteristic temperature, q is another numerical fit parameter depending on the experimental setup. α is a beam parameter, which is described by the degrees of freedom of the molecule f and the flux parameter s: $\alpha = sq - f/2$. The nozzle parameter can be calculated by

$$\Gamma = n_0 d^q T_0^{\alpha} \tag{2.35}$$

with n_0 the source density, T_0 the nozzle temperature and d the diameter of the nozzle. The source density can be obtained by using the ideal gas law:

$$n_0 = \frac{N_A}{R} \frac{p_0}{T_0} \tag{2.36}$$

with p_0 the stagnation pressure in the nozzle, R the universal gas constant and N_A Avogadro's number [26], [27], [28].

2.3.4 Low Energy Electron Diffraction

Low energy electron diffraction (LEED) experiments deal with the investigation of the crystal structure at the surface. This is done by shooting electrons at a target, where the electrons will scatter. The electron gun, which emits the electrons onto the target, consists of an arrangement of a cathode and an anode. Electrons will be emitted by the cathode and accelerated to the anode due to the constant potential difference. They will pass through a hole in the anode and the electron beam will be focused by electrostatic fields afterwards. Furthermore, these electric fields can be used to change the direction of the beam across the sample. The kinetic energy of the emitted electrons is quite low about 20-200 eV, which is responsible for the high surface sensitivity, because the interaction between the electrons and the surface becomes strong. There are two things that can happen to the electrons, when they meet the electrons of the sample. If the electrons experience an elastic scattering with the sample, this will result in a diffraction pattern, which corresponds to the surface structure. If the electrons are inelastically scattered they are going to loose their kinetic energy. The inelastically scattered electrons interact with the primary electrons of the crystal, which causes plasmon and phonon excitations as well as electron-electron interactions. The loss in kinetic energy is exponential and depends mainly on the inelastic mean free path. The inelastic mean free path defines the penetration distance of an electron till the intensity decreases by the characteristic factor 1/e. The advantage of the inelastic mean free path is that it's not too dependent on the chemical composition of the solid. This makes it possible to express a universal curve, which describes the inelastic mean free path for various elements (Fig. 2.11). The range of the inelastic mean free path is only some Å and therefore a few atomic layers can be sampled.

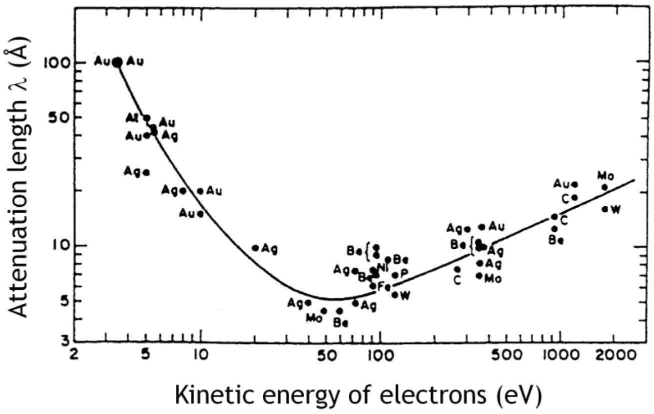

Figure 2.11: Universal curve of the inelastic mean free path of electrons [29, p.415].

The patterns, which are obtained from the elastically scattered electrons, can be described by the Ewald sphere. The electron beam is described as a plane wave with the de Broglie wavelength:

$$\lambda = \frac{h}{\sqrt{2mE}} \tag{2.37}$$

with Planck's constant h, m the mass of the electron and the kinetic energy E of the electrons, which can be varied. The Ewald sphere can be constructed on the surface (Fig. 2.12) with the radius of $\frac{1}{\lambda}$, therefore the reciprocal space of the lattice will be investigated. In case of the 2-dimensional lattice, the reciprocal lattice spots become rods. The intersection between these rods and the Ewald sphere determine constructive interference and Bragg's law is fulfilled. After the scattering process, the electrons travel towards the LEED screen. The LEED screen typically contains three hemispherical concentric grids and a fluorescent screen (Fig. 2.12). The first grid and the sample itself are grounded to suppress unwanted electrostatic fields between the detector and the sample which will disturb the experiment. The second grid is on negative potential to filter out inelastically scattered electrons. The screen has a positive applied voltage to accelerate the elastically scattered electrons towards the fluorescent screen for higher intensities [11, p.73-76], [18, p.47-51], [30, chap.4.2], [31, chap.3]. From the finally obtained reciprocal lattice, it is possible to determine the arrangement of the adsorbate with respect to the surface atoms. This reciprocal surface overlayer is described by the basis vectors of the overlayer

$$b_1^* = m_{11}^* a_1^* + m_{12}^* a_2^* \tag{2.38}$$

and

$$b_2^* = m_{21}^* a_1^* + m_{22}^* a_2^* \tag{2.39}$$

with m_{ij}^* scaling factors for the reciprocal lattice vectors and a_i^* the reciprocal lattice vectors. The matrix notation for these vectors would look like

$$b^* = M^* a^* \triangleq \begin{pmatrix} b_1^* \\ b_2^* \end{pmatrix} = \begin{pmatrix} m_{11}^* & m_{12}^* \\ m_{21}^* & m_{22}^* \end{pmatrix} \begin{pmatrix} a_1^* \\ a_2^* \end{pmatrix} \tag{2.40}$$

These relationships also apply to the real space lattice

$$b_1 = m_{11} a_1 + m_{12} a_2 \tag{2.41}$$

$$b_2 = m_{21} a_1 + m_{22} a_2 \tag{2.42}$$

with m_{ij} scaling factors for the basis vectors and a_i the basis vectors.

$$b = Ma \triangleq \begin{pmatrix} b_1 \\ b_2 \end{pmatrix} = \begin{pmatrix} m_{11} & m_{12} \\ m_{21} & m_{22} \end{pmatrix} \begin{pmatrix} a_1 \\ a_2 \end{pmatrix} \tag{2.43}$$

The matrices of the real space and the reciprocal lattice are connected by the relation

$$M(M^*)^T = 1 \tag{2.44}$$

Therefore the matrix notation for the real space lattice can be obtained by

$$M = \frac{1}{detM^*}\begin{pmatrix} m^*_{22} & -m^*_{12} \\ -m^*_{21} & m^*_{11} \end{pmatrix} \tag{2.45}$$

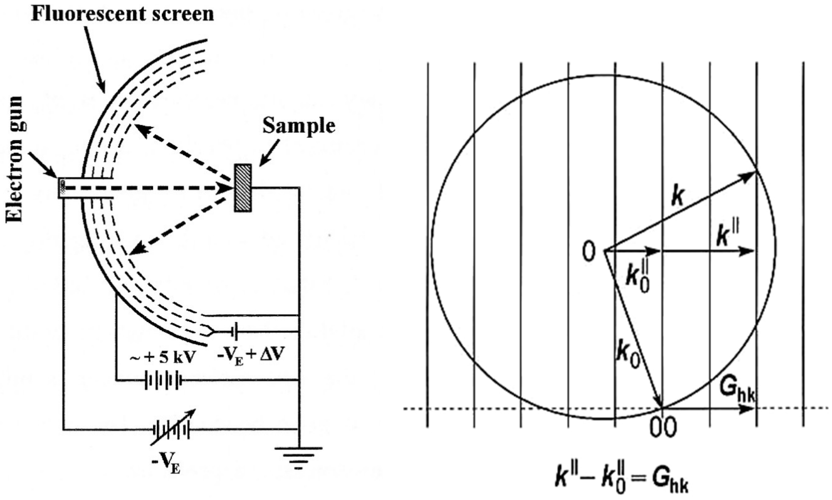

Figure 2.12: (Left) Schematics of the LEED apparatus [16, p.8], (right) Ewald sphere construction for a 2-d lattice. k_0 is the wavevector of the incident electron beam, k is the scattered electron beam and G is the lattice vector [18, p.49].

Furthermore, the distance between two adjacent atoms can be determined from the LEED pattern. The easiest way to describe the scattering of the electrons is by considering a one dimensional chain of atoms (Fig. 2.13). By comparing the backscattering wavefront of two adjacent atoms with distance a at a diffraction angle of θ to the surface normal, a path difference d will occur. The path difference $d = asin(\theta)$ can be identified with the Laue condition and determines constructive interference:

$$n\lambda = asin(\theta) \tag{2.46}$$

with n the diffraction order and λ the wavelength of the Ewald sphere [31, chap.3]. Then the kinetic energy of the beam for a certain pattern, where the first opposite lying spots start to appear on the screen, is measured. With the kinetic energy of the beam, the wavelength of the Ewald sphere can be calculated by using the de Broglie's equation (Eq. 2.37), which is also used to calculate the atomic distance:

$$a = \frac{\lambda}{sin(\theta)} \tag{2.47}$$

Another use of the obtained LEED pattern is to measure IV-curves, which give information on the local arrangement [11, p.77-80],[18, p.51-56].

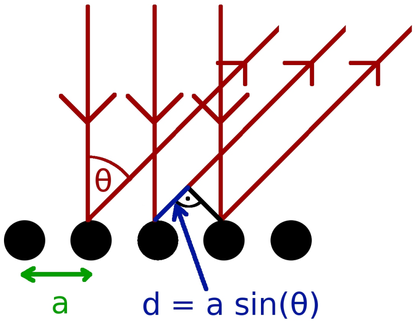

Figure 2.13: Schematics of the scattering of electrons on a one dimensional atomic chain. θ is the angle of the diffracted beam, a the atomic distance and d the path difference [32, p.23].

IV-curves

IV-curves can be obtained by the change in intensity as a function of beam energy, which, due to multiple scattering, is influenced by the local arrangement of the scatterer within the unit cell at the surface. Comparing the measured IV-curve with theoretical curves can provide accurate positioning information of the local arrangement. Doing so yields the R-Factor or Pendry-R-Factor that describes how well the theoretical data fits the measured IV-curve [18, p.57-59].

2.3.5 Auger Electron Spectroscopy

Auger electron spectroscopy (AES) is used to determine the chemical composition of surfaces. This spectroscopy technique aims to excite Auger transitions typically by electron bombardment. The energies of the electrons are in the range of 3-5 keV, whereas the measured energy of the Auger electrons is less than 1 keV. Because of this low energy, which results in an average mean free path of only some monolayers, AES is a surface sensitive technique. On the other hand, the energy of the primary electrons is high enough to eject core level electrons from the surface atoms. The vacancy is then filled up by a radiationless transition of electrons from a higher orbital. The energy of the transition is then released by ejection of a second electron, which is called Auger electron. This process has a higher probability to occur at atoms with lower masses [33, p.20-25]. When reaching atoms with higher mass numbers the radiationless transition is replaced by X-ray fluorescence and can be analyzed by X-ray photoemission spectroscopy (XPS) (Fig. 2.14). The kinetic energy of the Auger electron is dependent on the energy level of the atoms and is therefore unique for every atom, which makes it possible to get an elemental characterization of the surface. The measured energy is shifted compared to a neutral atom because the final state of the atom is still

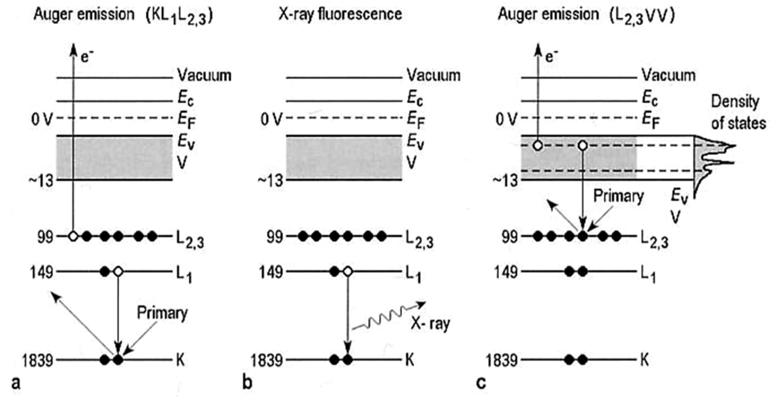

Figure 2.14: (a) and (c) are examples for Auger emissions where different core electrons due to electron bombardment are ejected. (b) is an example for an X-ray fluorescence process [18, p.83].

excited. The kinetic energy of the Auger electron can by calculated by:

$$E_{kin} = E_K - E_{L_1} - E_{L_{2,3}} - \Phi \tag{2.48}$$

with E_K, E_{L_1} and $E_{L_{2,3}}$ the binding energies of the K, L_1 and $L_{2,3}$ orbital and Φ the work function to bring the electron from the Fermi level to the vacuum level [18, p.82-83], [34, p.42-45].

The most basic technique to detect the Auger electrons is to use the same fluorescent screen of the LEED apparatus (Fig. 2.12 left side). This is called the retarding field analyzer (RFA) because of the produced field of the concentric hemispherical grids, which filters out unwanted electrons and accelerate it towards the fluorescent detector screen. The advantage of this technique is its large solid angle over which electrons may be detected but it suffers great noise problems because it also detects electrons above a certain energy. Other detectors like the cylindrical mirror analyzer (CMA) and the hemispherical sector analyzer (HSA) overcome this problem. The CMA consists of two concentric cylinders, with the outer cylinder at negative and the inner cylinder on earth potential. This will result in an electrostatic field, which sorts out undesired kinetic energies, although not only Auger electrons will pass but also other emitted electrons with similar kinetic energies. The HSA has an arrangement of a pair of concentric hemispherical electrodes. In between those electrodes there is a gap for the electrons to pass through. Those electrodes have a potential difference, where the outer one is more negative than the inner one. The two potentials allow only electrons with a certain energy to pass through the system [35, p.408-410].

Quantitative analysis of the obtained signal from Auger experiments is possible though it's very complicated. Not only elastic and inelastic scattering, but also other processes like backscattering can occur during an Auger experiment. The obtained signal is a combination of all of these quantities but the Auger transition is responsible for the peaks of the signal. This motivates an approximate chemical composition analysis by comparing the relative change of the peak intensities before and after a sticking experiment. The concentration of a chemical component

A in the sample can be determined by [36, p.127]:

$$x_A = \frac{I_A/s_A}{\sum\limits_i I_i/s_i} \tag{2.49}$$

with I the peak intensity at a certain energy, s the relative sensitivity factor and the subindex i marks the chemical component. The peak intensity can be obtained by calculating the peak-to-peak ratios for certain elements [33, p.233-239], [35, p.418-420].

2.3.6 Thermal Desorption Spectroscopy

Thermal desorption spectroscopy (TDS) or also known as thermal programmed desorption (TPD) is a technique to determine the desorption energy and the heat of adsorption on the surface. After an adsorption cycle, the sample is heated up at a constant rate so that the adsorbed molecules desorb from the surface, while the sample faces a QMS to detect the desorbed molecules. During the heating process the molecules will desorb at certain temperatures, which results in a peak in the QMS signal. Those peaks describe the order of desorption, which gives information how the molecule initally adsorbed on the surface (Fig. 2.15). In case of first order desorption the whole molecule was adsorbed on the surface. It can be identified if the peak position remains constant at a certain temperature for different pre-coverages of the material. In the case of second order desorption the molecule dissociated during the adsorption process. For second order desorption the peak position shifts for different amount of adsorbed molecules but the shape remains in a Gaussian like form. If during a TDS experiment the heating rate β is chosen to be fast enough, no readsorption will occur and the desorption energy can be calculated by applying the Arrhenius equation which results in the Polanyi-Wigner equation [11, p.213-218]:

$$r_{des}(t) = -\frac{d\Theta}{dt} = \nu_n \theta^n exp(-\frac{E_d}{k_B T}) \tag{2.50}$$

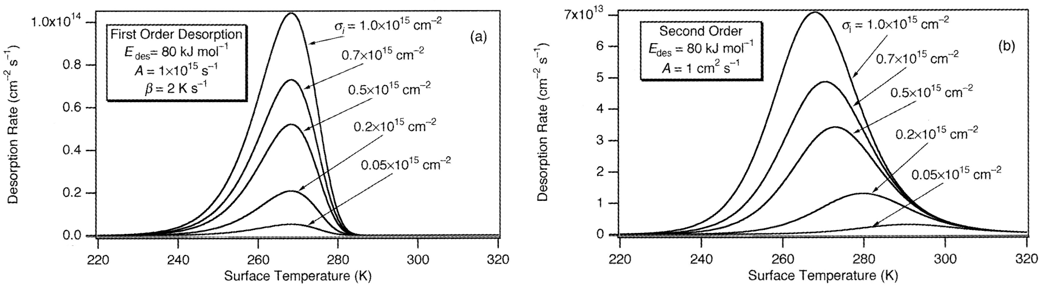

Figure 2.15: (a) First order desorption spectra with different initial coverages. The position of the peak always remains at the same temperature. (b) Second order desorption spectra. The position of the peak shifts at higher coverages but the symmetric shape of the peak remains [11, p.219].

with r_{des} the desorption rate, t the time , Θ the coverage, T the temperature, E_d the desorption energy, n the order of desorption, ν the frequency factor, and k_B the Boltzmann constant. In order to obtain the desorption energy, the Polanyi-Wigner equation has to be derived by the time and set equal to zero. It should be noticed for TDS experiments that the temperature T and the coverage Θ are time dependent:

$$0 = n\nu_n\theta^{n-1}exp(-\frac{E_d}{k_BT})\frac{d\Theta}{dt} + \frac{E_d}{k_BT^2}\underbrace{\nu_n\Theta^n exp(-\frac{E_d}{k_BT})}_{-\frac{d\Theta}{dt}}\underbrace{\frac{dT}{dt}}_{\beta} \tag{2.51}$$

The resulting equation can be transformed into:

$$\frac{E_d}{k_BT_p^2} = \frac{n\nu_n}{\beta}\Theta^{n-1}exp(-\frac{E_d}{k_BT_p}) \tag{2.52}$$

with T_p the peak temperature. For first order desorption this equation results in

$$\frac{E_d}{k_BT_p^2} = \frac{\nu_1}{\beta}exp(-\frac{E_d}{k_BT_p}) \tag{2.53}$$

and for second order desorption

$$\frac{E_d}{k_B T_p^2} = \frac{2\nu_2}{\beta}\Theta exp(-\frac{E_d}{k_B T_p}) \tag{2.54}$$

Redhead simplified the equation for first order desorption by showing that the desorption energy is related to the peak temperature [11, p.218-221]:

$$E_d = k_B T_p(\ln{(\nu T_p/\beta)} - 3.46) \tag{2.55}$$

which makes it possible to directly calculate the desorption energy of first order peaks.

3 Experimental Setup

3.1 The Vacuum Apparatus and Sample Preparation

Three vacuum chambers were used for the conducted experiments: the preperation chamber, the analysis chamber and the molecular beam (MB) chamber (Fig. 3.1). The sample used for the experiments was bulk cleaned and heat treated already inside the vacuum chamber. So additional evacuation and outbaking was omitted. The sample itself was a round plate with a radius of 6 mm. It was made of ferritic stainless steel, had 17 % Cr content inside the bulk and it was manufactured by "Metal Crystals & Oxides Ltd". The surface itself was single crystal, which was prepared in a Fe-17Cr(100) structure. This sample was mounted by 4 Mo clips on the sample holder (Fig. 3.2). The vacuum inside the preparation chamber with an average pressure of $2{*}10^{-10}$ Torr was created by a rotary vane and a turbomolecular pump. In the preparation chamber, the sample was cleaned by Ar-Ion sputtering before every experimental run. The purity of the used Ar was a scientific grade (6.0) and the Ar was produced by "Oy Aga Ab". The cleaning was done by letting Ar into the chamber through an ion gun, which was located on the lower backside of the chamber. The inflowing gas was set to a certain constant gas flow till the pressure inside the chamber reached $2.3 * 10^{-6}$ Torr, which was measured by an ion gauge (Controlling unit: Fig. 3.1 upper left part of (b)). Afterwards, the ion gun was turned on by a controlling unit (Fig. 3.1 (II)). The argon ions got a kinetic energy of 1 keV and a target current of about 13 μA. The sample was sputtered for 10 minutes before the gun was turned off. Then the Ar gas was pumped out of the chamber and the sample was transferred into the analysis chamber, where a rotary vane pump and a turbomolecular pump were responsible for the vacuum inside the analysis chamber. The resulting pressure was $9 * 10^{-11}$ Torr in average. Now the sample was annealed at a constant temperature for 10 minutes. The surface of the sample could be prepared in different ways depending on the annealing temperature. Therefore, it was annealed either at 900 K or 970 K for one experimental run. The pressure upon annealing was approximately $2 * 10^{-9}$ Torr. At 900 K the surface of the sample was more enriched with nitrogen, whereas at 970 K the surface became more carbon enriched. The heating of the sample was done resistively by tungsten wires behind the sample (Controlling unit: Fig. 3.1 (I), Sample holder: Fig. 3.2). Since this procedure includes very high temperatures, the sample holder had to be cooled by liquid nitrogen to prevent damage. After the annealing process was finished, the sample surface was clean and could be used for investigations.

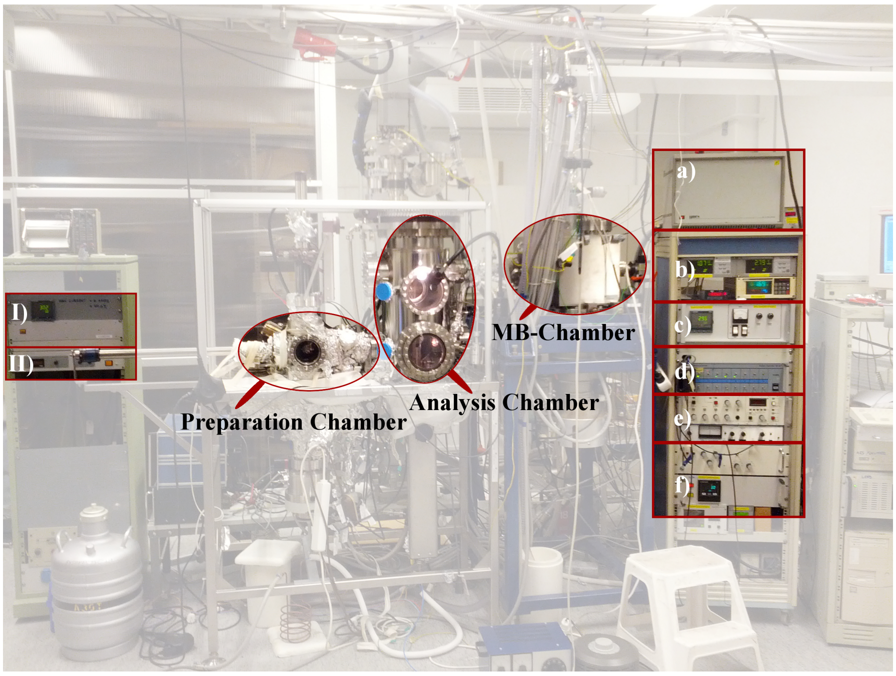

Figure 3.1: Experimental setup for the measurements. The apparatus consists of three vacuum chambers: the Preparation Chamber, the Analysis Chamber and the MB-Chamber. On the left and right side of the apparatus are controlling units and measuring devices.

In the beginning of every experimental run water was adsorbed on the surface by using a supersonic molecular beam, hence the MB-chamber was connected with the

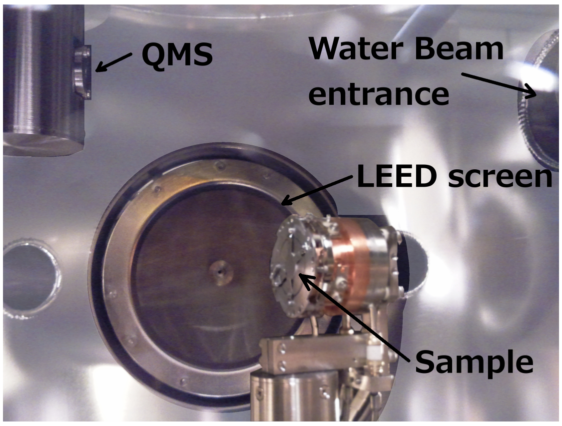

Figure 3.2: Photograph of the sample holder, LEED screen, QMS and the connection to the MB-chamber. The sample with its holder is mounted onto the copper block. The resistive heating of the sample is done by tungsten wires, which are located behind the sample.

analysis chamber by a gatevalve, which was open during an adsorption experiment. Since the gatevalve couldn't open fast enough for a King and Wells experiment, a shutter was placed in the beamline to release the beam on the sample as quickly as possible (Controlling unit: Fig. 3.1 (d)). To characterize the kinetic energy of the beam by a TOF measurement, a removable chopper could be placed in the beamline. The placement of the gatevalve, the shutter and the chopper disc can be seen in figure 3.3. Furthermore, the stagnation pressure inside the nozzle and the pressure in the MB-chamber and the analysis chamber was measured by ion gauges (Controlling units: Fig. 3.1 lower left of (b) for the ion gauge behind the nozzle and lower right of (b) for the ion gauge inside the MB-chamber and upper right part of (b) for the ion gauge inside the analysis chamber). The nozzle could also be heated up to 700 K resistively (Controlling unit: Fig. 3.1 (f)). The signal of the water was measured by a QMS, which was located on the opposite wall of the connection between the MB-chamber and the analysis chamber (QMS: Fig. 3.3, Fig. 3.2 and its controlling unit: Fig. 3.1 (a)). The vacuum inside the MB-chamber was produced by a rotary vane and an oil diffusion pump. An additional turbomolecular pump was responsible for the vacuum inside the collimation chamber, which is actually located between the nozzle and the skimmer, before the beam enters the MB-chamber. This turbomolecular pump had to be turned on full speed during every King and Wells experiment because otherwise the effusive background would have been higher.

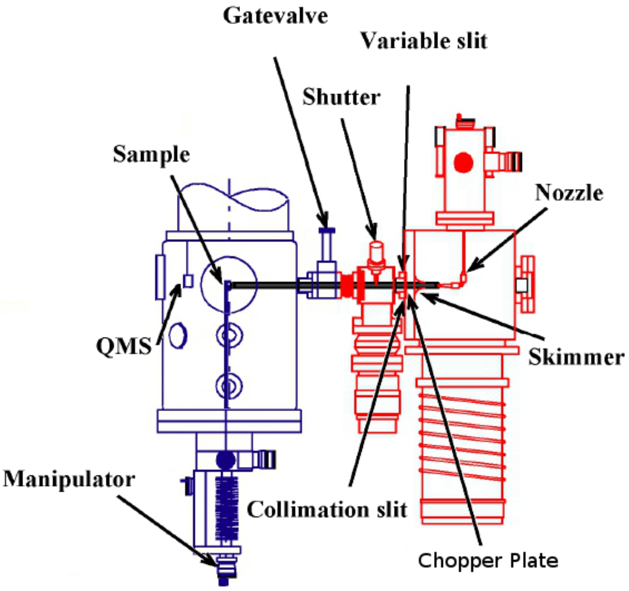

Figure 3.3: Schematics of the Analysis Chamber and the MB-Chamber. [16, p.6]

The further procedure consisted either of measuring LEED and AES or making a TDS experiment. After AES experiments the surface would experience heavy electron bombardment which changes the chemical composition of the surface and would make a TDS experiment after an AES experiment useless. During LEED and AES measurements the LEED screen on the back of the analysis chamber (Fig. 3.2) was brought closer to the sample holder to conduct these measurements, since both experiments utilize the same apparatus (Controlling unit: Fig. 3.1 (e)). This also means that a retarded field analyzer was used for the AES experiment. The TDS experiment on the other hand only needed the resistively heating mechanism of the sample holder and the QMS.

3.2 Generation and Characterization of the Supersonic Water Beam

The generation and characterization of the molecular water beam was probably the most important part for this thesis and for further investigations. The characterization of the water beam can be divided into TOF experiments, determination of the average cluster size inside the beam and calculating the flux of the beam. The TOF experiments are responsible to obtain the translational energy of the beam, the terminal temperature and the seeding ratio of water to helium. The calculations for the cluster size inside the beam are necessary for the determination of the flux and determine the necessity to consider additional effects. The obtained flux will be used in chapter 4.1 to get the dependency of the sticking coefficient to the exposure of the surface to water molecules.

3.2.1 Generating the Water Beam

For establishing a supersonic water beam, it is necessary to pressurize the nozzle of the MBSS system with water vapor. Therefore, a reservoir with deionized water was attached to the supply pipeline behind the nozzle. In order to guarantee the cleanliness of the deionized water, the reservoir was cleaned with ethanol and ultrasonically before the installation.

After the installation the reservoir was cooled by liquid nitrogen so it was possible to pump away volatile impurities. Such a procedure is called a freeze–pump–thaw cycle [37]. Then a thermocouple for measuring the reservoir temperature, heating tape for the evaporating process and aluminum foil for insulating the system was applied on the reservoir (Fig. 3.4). Before water vapor could be produced by boiling the water in the reservoir at a temperature of about 90 °C, the pipeline between the nozzle and the reservoir had to be heated up already as well as the nozzle itself. Otherwise the water would have condensed on the walls of the pipeline and the chamber behind the nozzle. Therefore, heating tapes were applied to the supply pipeline and kept at a temperature of about 110 °C. The kinetic energy of the released supersonic water was either controlled by adjusting the temperature of the nozzle or by seeding the water beam with lighter molecules like in our case helium. Adjusting the temperature of the nozzle was limited because below a certain temperature at about 500 K the beam couldn't be established. This limit was mainly due to a partly blocked nozzle, which affected the nozzle conditions in such a way that no supersonic water beam could have been established below this temperature [38].

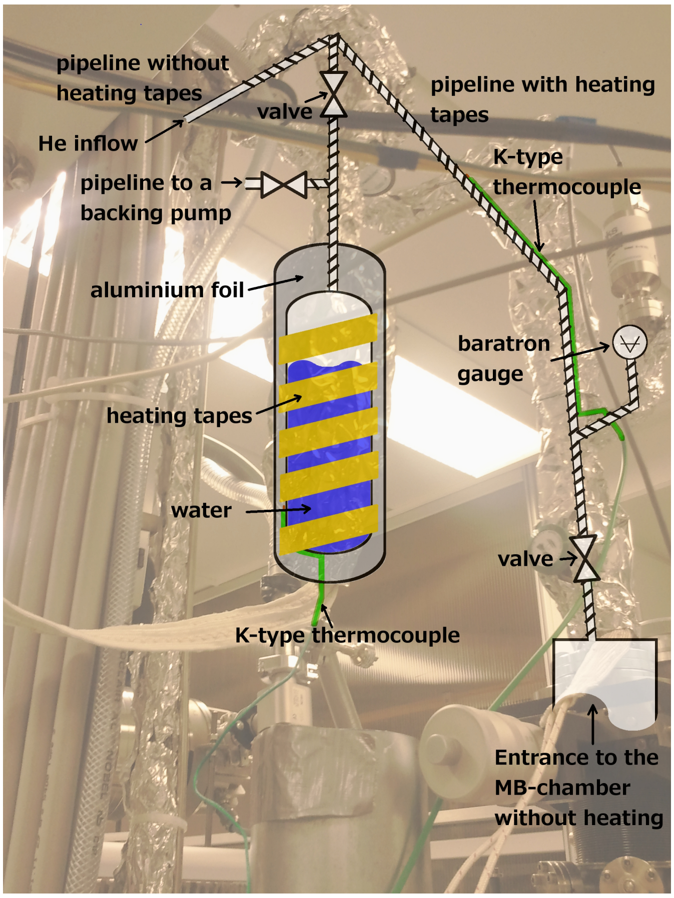

Figure 3.4: Construction of the water reservoir with overlaying schematics.

The upper limit of the nozzle was 700 K due to material properties of the nozzle. In the executed experiments the temperature of the nozzle was kept at 700 K to guarantee the highest measured intensity as well as the best stability for the beam. A region between the supply pipeline and the nozzle that could not be heated directly, had a tremendous influence on the high nozzle temperature as well. This region was located between the entrance of the MB-chamber and the nozzle itself. Heating this region would involve enhancing the MB-chamber but it was compensated by the high nozzle temperature so that water wouldn't condensate in this area.

As for the seeding ratio, it was kept at the same level but this was due to time limitations for the experiments. The He inflow was controlled by a mass flow controller, which kept the inflow at 4 standard cubic centimeter per minute (sccm). In every experimental run, first the nozzle was pressurized with He at about 420 Torr, before water was evaporated and added to the stagnation pressure. Since there was only a gatevalve between the water reservoir and the supply pipeline, the water inflow could not be controlled as easy as He. Therefore, the evaporation process and the water gas inflow had to be controlled in such a way that the stagnation pressure reached about 700 Torr. This also involed pumping away water vapor, especially because a glass reservoir was used and pressures above 740 Torr could have caused damage to the reservoir. Additionally, it was necessary to wait for about an hour to let the beam stabilize.

3.2.2 Determination of the Kinetic Energy and the Water to Helium Ratio of the Beam

The kinetic energy was determined by TOF measurements. During those measurements the sample holder was below the beamline, whereas the chopper plate was placed in the beamline and turned on. The rotating disc consists of two narrow slits, which will chop the water beam. When one of the slits releases the water beam, which will be measured by the QMS, the other slit releases a triggering signal to a photodetector [39, p.18-20], [40, p.15-18]. The measured sequence for the pulsed water beam is only a few micro seconds long and typically thousands of pulses are measured. To obtain a coherent TOF distribution, a Multi Channel Analyzer (MCA) card was used, which will combine the measured sequences [22, p.14-53]. In the case of the used water beam 40000 pulses were necessary to get a good intensity-noise ratio for evaluation. But before the obtained data could be analyzed, the TOF system had to be calibrated according to the correspondig chapter 2.3.3. Therefore, the measured time by the TOF experiment consists of the real time of flight and additionally of two delays from the trigger and the QMS detector (Eq. 2.20) For calculating the detector delay as described in equation 2.21, two nobel gases argon and krypton with the mass-charge ratios $(m/q)_{Ar} = 40$ and $(m/q)_{Kr} = 84$ were used. This resulted in a trigger delay of $78\,\mu$s for Ar and $82\,\mu$s for Kr with an average of $(80 \pm 3)\,\mu$s. The constant K for the detector delay was 11.9 for Ar and 8.9 for Kr. The average was 10.4, which resulted in a detector delay of $(44 \pm 2)\,\mu$s for water molecules with a mass-charge ratio of 18. This means that the measured time for water is $(124 \pm 5)\,\mu$s longer than the real flight time (Fig.3.5 left side).

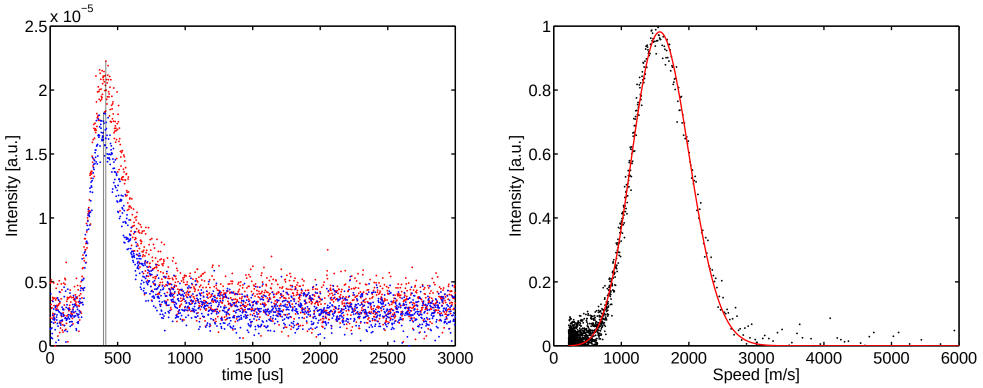

Figure 3.5: Left figure: Two examples for TOF measurements before and after a sticking experiment. The time has already been adjusted to the real time according to Eq.[2.20]. Due to the shape of the narrow distribution it indicates that a supersonic molecular beam and not an effusive beam was created for the experiments.
Right figure: From one of the adjusted TOF measurement calculated speed distribution of water molecules. The distribution is normalized and the red line is a fit for a shifted Maxwell distribution according to equation 3.2.

After the trigger and the detector delay is subtracted from the measured time distribution of the TOF data, it can be transformed into a velocity distribution through $v = L/t_{real}$ with $L = 0.66\,\mathrm{m}$ the flight path of the molecules, which is the distance between the nozzle and the QMS. The velocity distribution can be described by a shifted Maxwell-Boltzmann distribution of the form [19, p.180]:

$$f_{MB}(v) \propto v^3 exp(-a(v - v_0)^2) \tag{3.1}$$

with v_0 the mean velocity and some constant a.

The used QMS is density sensitive, whereas the previous expression is for flux sensitive detectors [19, p.180]. This means the used function has to be divided by v. Since time is measured instead of velocity, it affects the Jacobian. The measured function changes to $g(t) = f(t)v^2$, where v^2 is the part from the Jacobian. Taking these considerations into account the resulting expression is:

$$f_{MB}(v) \propto v^4 exp(-a(v - v_0)^2) \tag{3.2}$$

This was fitted numerically to the velocity distribution (Fig. 3.5 right side) obtained from the measured TOF data by using Matlab's nlinfit function.

The maximum intensity of the distribution corresponds to the average velocity of the molecules, which was taken to calculate the translational energy E_t of the beam according to equation 2.25. The half width of the numerical fit and the equation 2.29 was used to determine the terminal temperature T_{term}. The calculated translational energies and terminal temperatures from the TOF measurement for various experiments can be looked up in table 3.1. Averaging and forming the standard deviation over those results give an average energy of $E_t = [248 \pm 17]\,\mathrm{meV}$ and an average terminal temperature of $T_{term} = [429 \pm 26]\,\mathrm{K}$. The inevitable high terminal temperatures are problematic for the experiment because the speed distribution isn't as narrow as it should be, which is desired by MBSS methods.

After obtaining the translational energy of the supersonic water beam it was possible to determine the percentage of water inside the beam. By using equation 2.19, the average molecular weight of the beam was calculated, which can also be described by

$$W_{avg} = (x_{H_2O} W_{water} + (1 - x_{H_2O}) W_{He}) \tag{3.3}$$

Table 3.1: Obtained translational energies and terminal temperatures of the TOF experiment and the calculated percentage of water inside the beam
p_{stag} ... adjusted stagnation pressure inside the gas chamber
t_{meas} ... measured peak position in the TOF measurement.
t_{real} ... real time of flight (according to eq. 2.20)
E_t ... translational energy of the water (according to eq. 2.25)
T_{term} ... terminal temperature (according to eq. 2.29)
W ... average molar mass of the molecular beam (according to eq.2.19)
x_{H_2O} ... calculated percentage of water inside the molecular beam (according to eq.3.3)

p_{stag} $[Torr]$	t_{real} $[\mu s]$	t_{meas} $[\mu s]$	E_t $[meV]$	T_{term} $[K]$	W [g/mol]	x_{H_2O}
616	545	421	229	389	9	34
700	533	409	243	432	7	22
713	534	410	242	438	7	25
728	506	382	279	472	6	13
713	523	399	256	431	7	21
723	514	390	268	448	6	16
694	525	400	254	434	7	21
708	523	398	256	447	6	18
715	543	418	232	394	9	36
678	549	425	225	408	9	34

with x_{H_2O} the percentage of water inside the beam. The obtained water percentages can be looked up in table 3.1. The average water percentage in the molecular beam resulted in $x_{H_2O} = [24 \pm 8\,]\%$

3.2.3 Formation of Clusters

The tendency of water to form clusters makes it necessary to investigate the cluster size of water molecules for pure water beams. According to chapter 2.3.3 the determing factors for calculating the cluster size for molecular beams are the source density n, the pressure p and the temperature inside the nozzle T_{nozz} as well as the diameter of the nozzle d, which was $d = 40\,\mu$m. For every experimental run the temperature of the nozzle was kept at $T_{nozz} = 700\,$K and the pressure roughly at $p = 700\,$Torr. This leads to a source density of $n = 9.66 * 10^{24}\,$molecules/m^3

according to equation 2.36. These parameters define the nozzle parameter Γ, which is described by equation 2.35. As for the parameter $\alpha = sq - f/2$ changes to $\alpha = q - 3$ because for water molecules the degrees of freedom $f = 6$ (3 translational and 3 rotational degrees of freedom) and $s = 1$ for axial symmetric flows. The parameter $q = 0.634$, which is a fit-parameter and was taken from studies on water clusters by Bobbert et al [27, p.188]. From this study also the characteristic radius $r_{ch} = 3.19\,\text{Å}$ and the characteristic temperature $T_{ch} = 5684\,\text{K}$ was taken to calculate the characteristic scaling parameter $K_{CH} = 3.84 * 10^{-13}\,\text{m}^{\text{q}-3}\text{K}^{\alpha}$ according to equation 2.34. After calculating $\Gamma = 2.92 * 10^{15}\,\text{m}^{\text{q}-3}\text{K}^{\alpha}$ the dimensionless parameter $\Gamma^* = 75.95$ could be calculated using equation 2.33. Finally, with Γ^*, equation 2.32 and the fit-parameters $D = 11.60$ and $a = 1.886$, which were also taken from the study on water clusters by Bobbert et al [27, p.188], the average cluster size $< n >$ could be determined. But this resulted in an average cluster size of $< n >= 0.1$ because Hagena's law cannot be applied for Γ^* below a certain value [41]. Nonetheless, the low value for Γ^* indicates that the cluster size must be very small and it can be expected that only dimers or trimers will be formed.

3.2.4 Flux of the Beam

The flux of the beam was determined by a conducted water sticking experiment (Fig. 3.6) since there was no calibrated leak for water available. The procedure of such an experiment will be explained in chapter 4.1. During this experiment the surface temperature of the sample was $T_S = 150\,\text{K}$. After the shutter was opened, the QMS signal took about 16 seconds until it starts to rise. The point, where the signal started to rise was determined by the intersection of an exponential and a linear fit.

It can be assumed that during this time one monolayer was filled because every incoming water molecule will be adsorbed on the surface. Only after the first wetting ice layer is formed, the sticking coefficient starts to decrease. This can be explained by the wetting of water on metal surfaces. Water and metal surfaces have a similar binding energy like water and bulk ice. Therefore, the formation of an initial 2-D structure followed by 3-D structures (Stranski-Krastanov) is more

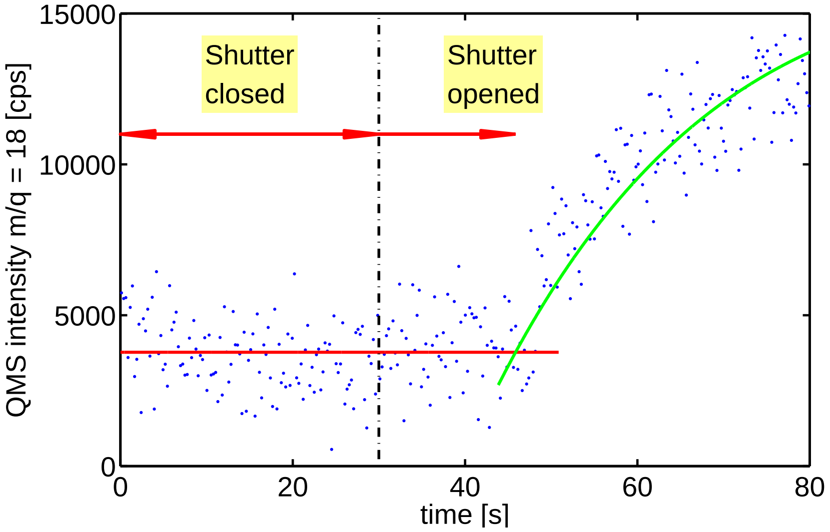

Figure 3.6: Water sticking experiment to calculate the flux of the beam. It took about 16 seconds till the monolayer was filled and the QMS signal started to rise. The green line is an exponential fit, whereas the red line is a linear fit. The intersection determines the point, where the signal started to rise.

favorable than a continuous ice film (Franck van der Merve). This means that the adsorption of water at a metal surface is precursor-mediated, which is possible at the used surface temperature due to the mobility of water. Water will preferable adsorb on upper side of steps and then grow from the lower step edge. The precursor-mediated adsorption is responsible for the independence of the sticking probability until the surface is saturated with one monolayer of water [42, p.388-389].

Now the flux can be calculated [43]:

$$F = \frac{d\rho}{t} \tag{3.4}$$

with $d = 4\,\text{Å}$ the thickness of a single monolayer of water [44, table IV],[45, p.5], $t = 16\,\text{s}$ the time it took till this monolayer was filled and $\rho = 917\,\text{kg/m}^3$ the density of ice at $0\,^\circ\text{C}$ [46]. With $d\rho$, the Avogadro constant $N_A = 6.022 * 10^{23}\,\text{mol}^{-1}$ and the molar weight of water $W = 18\,\text{g/mol}$ the density of one monolayer of water can be determined, which is $\tilde{\rho}_{ML} = 1.23 * 10^{15}$ molecules/cm^2. Dividing this expression by the time it takes to form the monolayer, the flux of the beam can be calculated: $F = 7.73 * 10^{13}$ molecules/cm^{2}s.

Additionally, the area, which the beam hits, was measured before the actual measurement series. This was done to determine the area that the beam affects. For this measurement O_2 was adsorbed on the surface. Afterwards a LEED measurement was conducted and the surface structure with the adsorbed oxygen was observed. Inside the beam hitting area, no LEED pattern could be observed due to the adsorbed oxygen, which was lacking the long range order. Outside of the beam hitting area, the LEED pattern was visible again. Then the position of the sample was changed until the region, where the oxygen adsorbed, was determined. This resulted in a beam radius of $r = 0.4\,\text{cm}$ and a beam area of $A = 0.503\,\text{cm}^2$ compared to the actual sample radius of $r = 0.6\,\text{cm}$ with a total area of $A = 0.905\,\text{cm}^2$.

4 Experimental Results and Discussion

4.1 Adsorption Kinetics and Dynamics

Adsorption kinetics of the sample were determined by conducting a King and Wells experiment according to chapter 2.3.3. Therefore, the chopper disc was removed from the beamline and the sample holder was placed inside it with the sample facing towards the incoming beam. The distance between the QMS to the sample was about 65 mm and the distance between the sample to the collimater slit was about 580 mm. Afterwards, the gatevalve between the analysis chamber and the MB-chamber was opened. The “sticking signal” for the adsorption was obtained by the following steps: The QMS measured 30 seconds of background intensity until the shutter was opened to release the beam into the analysis chamber. The sample adsorbed water molecules for about 360 seconds. Then the shutter was closed again. Furthermore, the downslope, which represents the desorption of molecules was measured for 240 seconds before the measurement was stopped. The same procedure had to be done for the back of the sample holder to obtain the “response signal”. The King and Wells measurement series was conducted for sample temperatures of 200 K, 323 K, 400 K, 523 K and 600 K. The experiments for 200 K, 523 K and 600 K couldn’t be evaluated for adsorption kinetics because the sample holder had to be cooled down by liquid nitrogen. The extreme cold surface of the sample holder resulted in the vanishing of the response signal due to adsorption of water on the surface of the sample holder during the measurement of the “response signal”. But the sticking experiments still could be used for further investigations in LEED, AES and TDS experiments.

The measured intensity had a background, which had to be eliminated by subtracting a linear fit from the measured points of the first 30 seconds and the last 220 seconds, so the fit wouldn’t interfere with the uptake and downslope area of the signal. The obtained sticking signals without the background can be seen on the left side of figure 4.1, 4.2, 4.3 and 4.4.

The difference between the “response signal” and the “sticking signal” represents the uptake area, which is an indication for adsorbed molecules and the sticking coefficient. The sticking coefficient can be calculated by equation 2.15. The still active uptake of the “response signal” can be explained by the strong interaction of water with steel parts in the chamber. The time dependence of the coverage can be calculated by using equation 2.16. The flux F of the water beam is needed in this calculation and was obtained in chapter 3.2.4 with a value of $F = 7.73 * 10^{13}\,\mathrm{molecules/cm^2s}$. The time dependent sticking coefficient can be plotted against the time dependent coverage resulting in the kinetics of the surface. The outcome can be seen on the right side of the figures 4.1, 4.2, 4.3 and 4.4. Due to the existing uptake of the “response signal”, the beginning of the calculated graphs show strange behavior. This motivates a linear fit to obtain the initial sticking coefficient by extrapolation. The points used for the linear fits were determined empirically and generally include the linear part after the beginning. Statistically better results can be achieved by forming the average of the calculated graphs with similar measurement conditions (figure 4.5). The average of the graphs was achieved by calculating the mean coverage and the mean sticking coefficient for each timestep. From the obtained graph the following initial sticking coefficients S_0 for different surface temperatures T_S and annealing temperatures T_A were calculated by using the linear fit in the beginning of each sticking curve:

- $S_0 = 0.34$ for $T_S = 323\,\mathrm{K}$ and $T_A = 900\,\mathrm{K}$
- $S_0 = 0.24$ for $T_S = 323\,\mathrm{K}$ and $T_A = 970\,\mathrm{K}$
- $S_0 = 0.35$ for $T_S = 400\,\mathrm{K}$ and $T_A = 900\,\mathrm{K}$

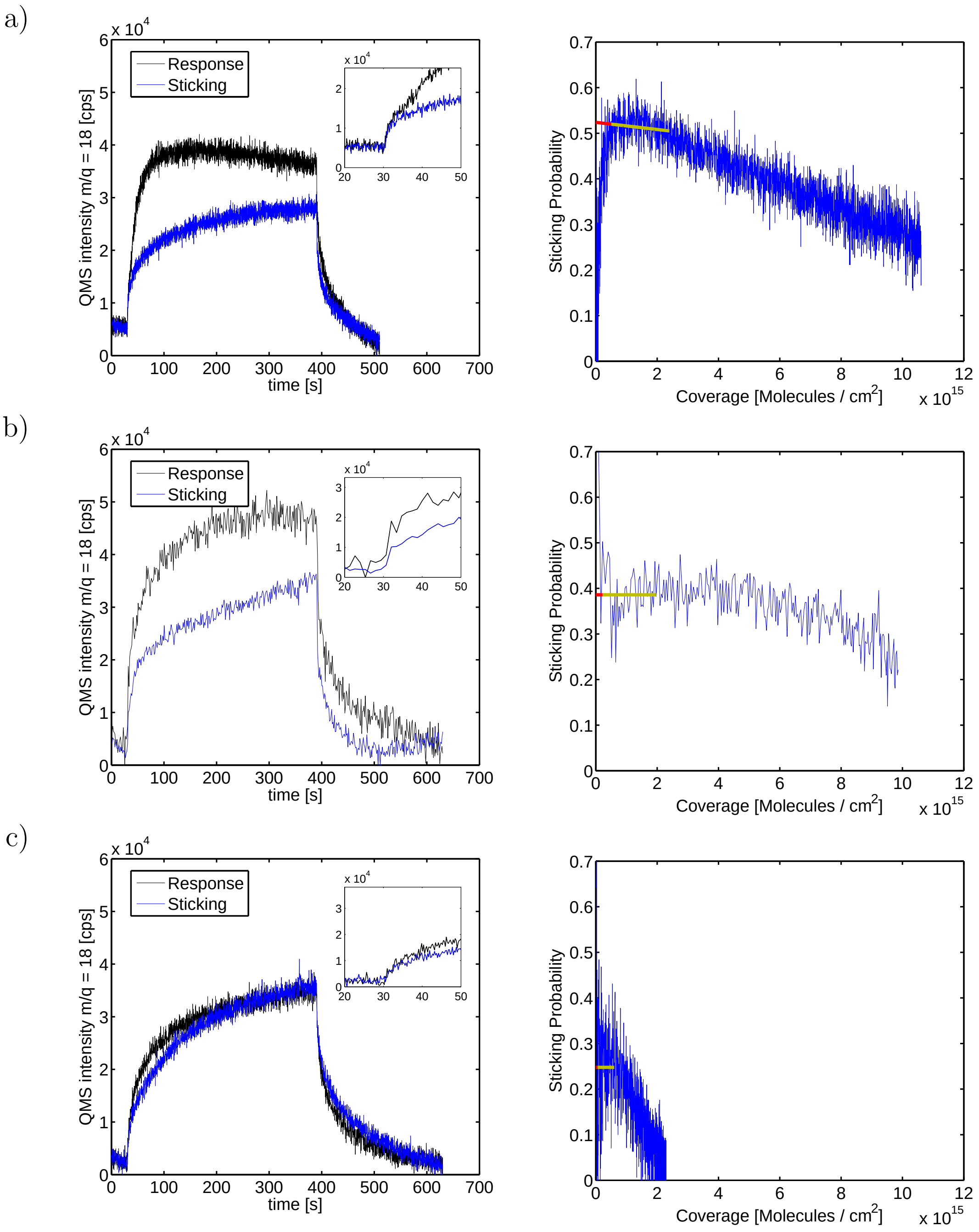

Figure 4.1: (Left column) Three different QMS signals of H_2O during MBSS measurements at the sample temperature of 323 K and annealing temperature of 900 K. The graphs at the upper right part of these figures show the beginning of the uptake area. (Right column) Evaluated sticking probability as a function of adsorbed molecules. The yellow line marks the region of a linear fit, which is used to obtain the initial sticking coefficient S_0 by extrapolation (red line). The initial sticking coefficients are: (a) $S_0 = 0.52$, (b) $S_0 = 0.39$ and (c) $S_0 = 0.25$.

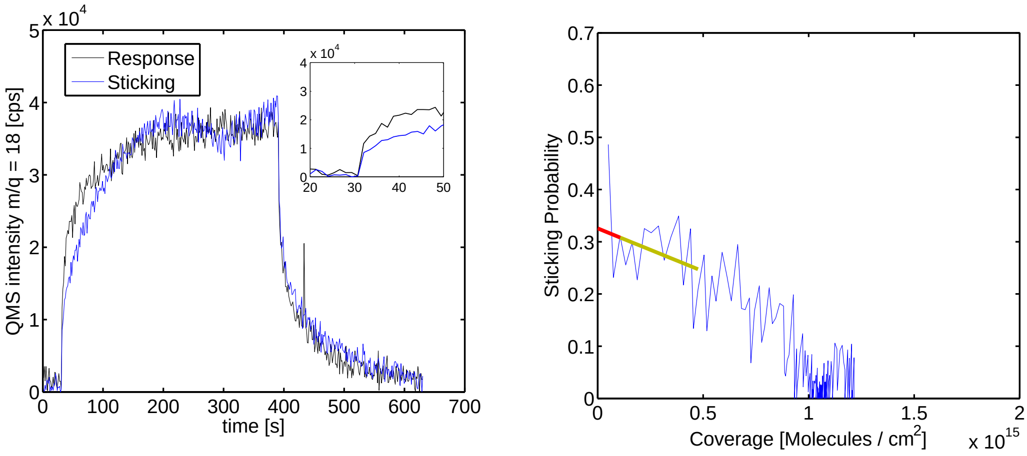

Figure 4.2: (Left side) QMS signal of H_2O during MBSS measurements at the sample temperature of 400 K and annealing temperature of 900 K. The graph at the upper right part of this figure shows the beginning of the uptake area. (Right side) Evaluated sticking probability as a function of adsorbed molecules. The yellow line marks the region of a linear fit, which is used to obtain the initial sticking coefficient S_0 by extrapolation (red line). The initial sticking coefficient is: $S_0 = 0.33$.

- $S_0 = 0.35$ for $T_S = 400\,\mathrm{K}$ and $T_A = 970\,\mathrm{K}$

The surfaces with a temperature of 323 K and different annealing temperatures show a constant sticking coefficient at the beginning of the adsorption experiment, indicating a pre-cursor mediated adsorption. Similar effects were shown by A. Hodgson et al [42, p.388-389] for the wetting of different metal surfaces. For a surface temperature of 400 K this behavior can be barely seen due to the few measuring points at the beginning of the experiment. A better resolution could have been achieved by a smaller beam flux and longer adsorption cycles but in due consideration of the intensity to noise ratio, which will increase with a decreasing flux.

Further experiments with this investigation technique would have consisted in changing the properties of the flux of the beam, changing the temperature of the surface and the duration of the adsorption experiment. By changing the seeding ratio and the temperature of the beam, the kinetic energy of the water molecules

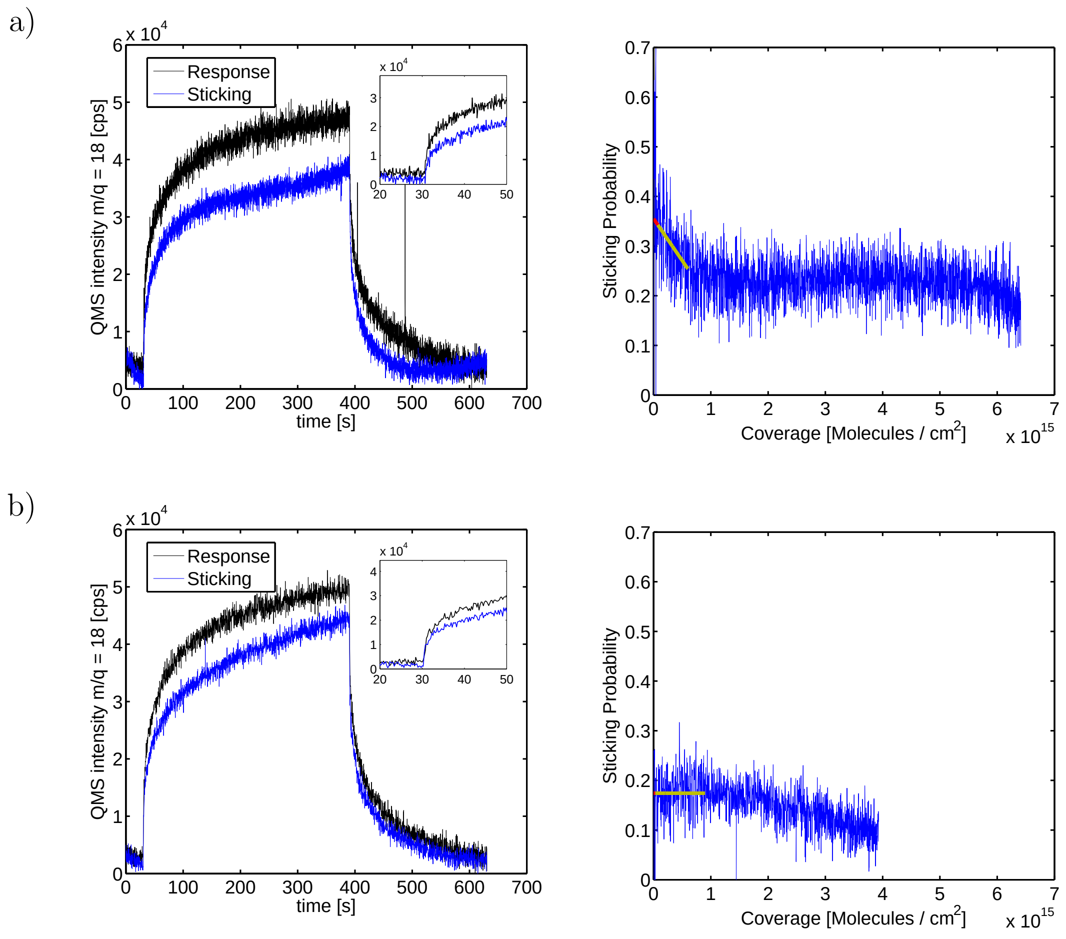

Figure 4.3: (Left column) Two different QMS signals of H_2O during MBSS measurements at the sample temperature of 323 K and annealing temperature of 970 K. The graphs at the upper right part of these figures show the beginning of the uptake area. (Right column) Evaluated sticking probability as a function of adsorbed molecules. The yellow line marks the region of a linear fit, which is used to obtain the initial sticking coefficient S_0 by extrapolation (red line). The initial sticking coefficients are: (a) $S_0 = 0.35$ and (b) $S_0 = 0.17$.

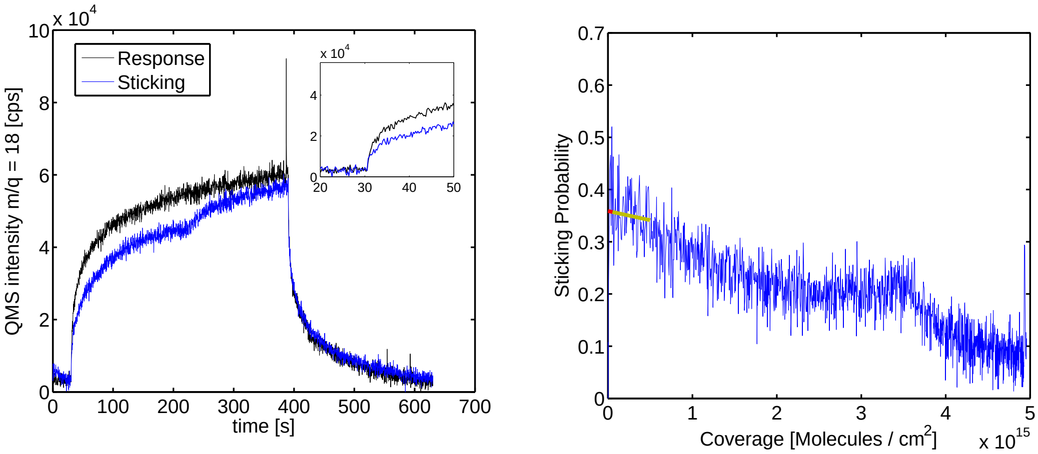

Figure 4.4: (Left side) QMS signal of H_2O during MBSS measurements at the sample temperature of 400 K and annealing temperature of 970 K. The graph at the upper right part of this figure shows the beginning of the uptake area. (Right side) Evaluated sticking probability as a function of adsorbed molecules. The yellow line marks the region of a linear fit, which is used to obtain the initial sticking coefficient S_0 by extrapolation (red line). The initial sticking coefficient is: $S_0 = 0.36$.

would have changed as well. Taking adsorption spectra for different kinetic energies give information on the whole PES, which includes occuring adsorption barriers and precursor states. The same procedure applies for different surface temperatures, which could only be recorded for 323 K and 400 K. The most important part to take care of in changing the surface temperature is not to change the conditions in the vacuum apparatus too drastically like cooling the sample holder with liquid nitrogen. The water molecules would have an additional possibility to adsorb, which interferes with the measurement. On the other hand, increasing the duration of adsorption reveals steady states for certain energies, which would only occur at a later stages in the adsorption process. Moreover, the experiment can be enhanced by taking the angular distribution of adsorption and desorption spectra [47], [48], which shows the effects of the surface structure on the bonding, though the effort is very high.

4.2 Desorption Spectra

After the adsorption experiment the sample was brought in front of the QMS for a TDS experiment. This ensures that the detector receives the desorbing molecules, while the sample is rapidly heated. For this experiment only one TDS spectrum could be recorded, whereas other recorded spectra with a start temperature of 323 K didn't show peaks for desorbing water. The adsorption experiment according to King and Wells for the investigated TD spectrum was conducted for a surface temperature of 150 K. The controlling unit though didn't allow to set the start temperature to 150 K. Therefore, the recording had to start at 200 K, which was the lowest temperature possible for the device. Then the sample was annealed up to 950 K. In the beginning of the heating process, the heating rate β was low but it changed roughly to $\beta = 3\,\mathrm{K/s}$. The whole recorded TD spectrum can be seen in figure 4.6, where two peaks can be observed. The adsorption temperature was so low that it can be assumed that the molecule didn't dissociate during adsorption, which means that the desorption obeys first order. The dissociation of water into OH groups, which then bind to the surface, usually occur around room temperature and higher temperatures. The typical desorption temperature for these second order desorption processes is above 600 K [49]. In our case the first peak appeared around 223 K representing weakly bonded ice clusters, whereas the second peak is the desorption of water molecules, which are directly bonded to the surface atoms.

Both peak positions were determined using polygonal fits on them and evaluating the maxima of those fits. This resulted in peak positions at $T_1 = 223\,\mathrm{K}$ for the first peak and $T_2 = 511\,\mathrm{K}$ for the second peak. By utilizing the approximation from Redhead (Eq.2.55), with a frequency factor of $\nu = 10^{13}\,\mathrm{s}^{-1}$ [49] and the temperatures obtained from the peak positions, the desorption energy of these two peaks can be determined. The resulting desorption energies are $E_{d,1} = 0.59\,\mathrm{eV}$ for the first and $E_{d,2} = 1.38\,\mathrm{eV}$ for the second peak.

According to the work of J. P. Joly et al [49] and the results on wetting metal surfaces by A. Hodgson et al [42, p.388-389], these peaks follow first order desorption because the surface temperature was too cold to enable dissociation of water

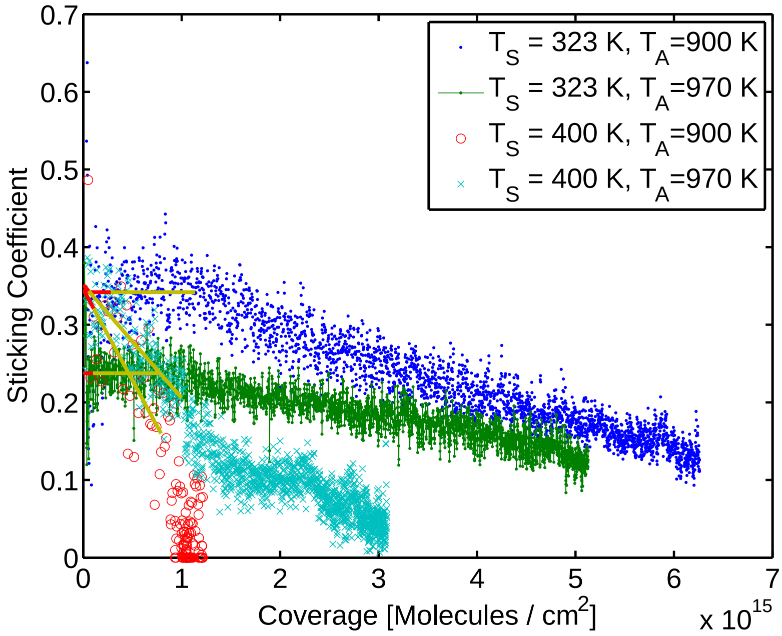

Figure 4.5: Sticking probabilities as functions of coverage for different setups (T_S...surface temperature and T_A...annealing temperature). The yellow lines mark the region of linear fits, which are used to obtain the initial sticking coefficient S_0 by extrapolation (red lines).

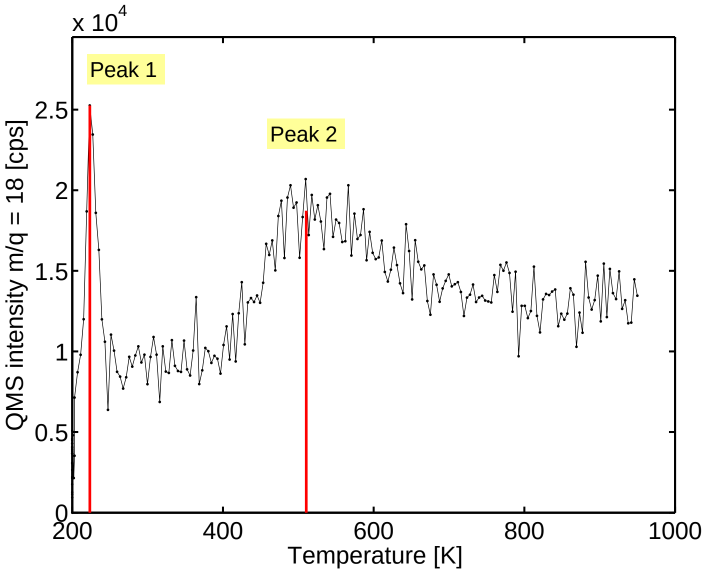

Figure 4.6: TD spectrum for a conducted adsorption experiment at the surface temperature of 150 K. The measurement started at 200 K due to the limited adjustment possibilities of the controlling unit. The maxima of the two first order peaks are marked with a red solid line.

molecules to OH groups. Other experiments at higher temperatures failed since the measured intensity of the desorption peaks couldn't surpass the noise ratio. Solutions of this problem would involve longer adsorption cycles and decreasing the distance between the QMS and the sample to make sure every desorbing molecule would reach the detector. Moreover, conducting TDS experiments after higher surface temperatures would reveal second order peaks around 750 K and 1000 K, which is comparable to the work of J. Joly et al [49]. Therefore, higher surface temperatures enables the formation of OH-layers on the surface.

There are two explanations that no peaks appeared for a surface temperature of 323 K for adsorption, whereas 150 K showed two peaks. One is that not enough water was adsorbed on the surface to surpass the noise of the desorption spectrum. The other one is that water dissociated further forming Cr-O layers, which have a very high bonding energy and can be proven by recording the mass charge ratios for H_2 in a TDS experiment [50].

4.3 Crystal Structure and Chemical Composition of the Surface

The crystal structure and the chemical composition of the surface were determined by utilizing the LEED apparatus. Therefore, the sample was brought close to the LEED screen. The distance was about 20 mm to ensure a good resolution of the scattered electrons from the surface. During these experiments the sample was grounded over the sample holder to eliminate electrostatic fields between the sample and the detector as well as avoiding the charging of the sample. The transfer between the LEED screen and the computer for the LEED patterns was done by utilizing a CCD (Charge-Coupled Device) camera on the back of the LEED screen. From the LEED patterns IV-curves were obtained by a special software. This software analyzes the intensity of the spots in the patterns. For AES measurements, which analyzes the chemical composition, the LEED apparatus was used as well. The LEED screen itself is a retarding field analyzer. The RFA is responsible for the great noise at lower kinetic energies for the detected electrons.

The primary electrons were accelerated to a kinetic energy of 28 - 198 eV for the conducted LEED experiments. In case of AES measurements the kinetic energy of the primary electrons was changed to 2.5 keV and the emission current was increased by increasing the filament current from 2.4 A for the LEED experiment to 2.6 A.

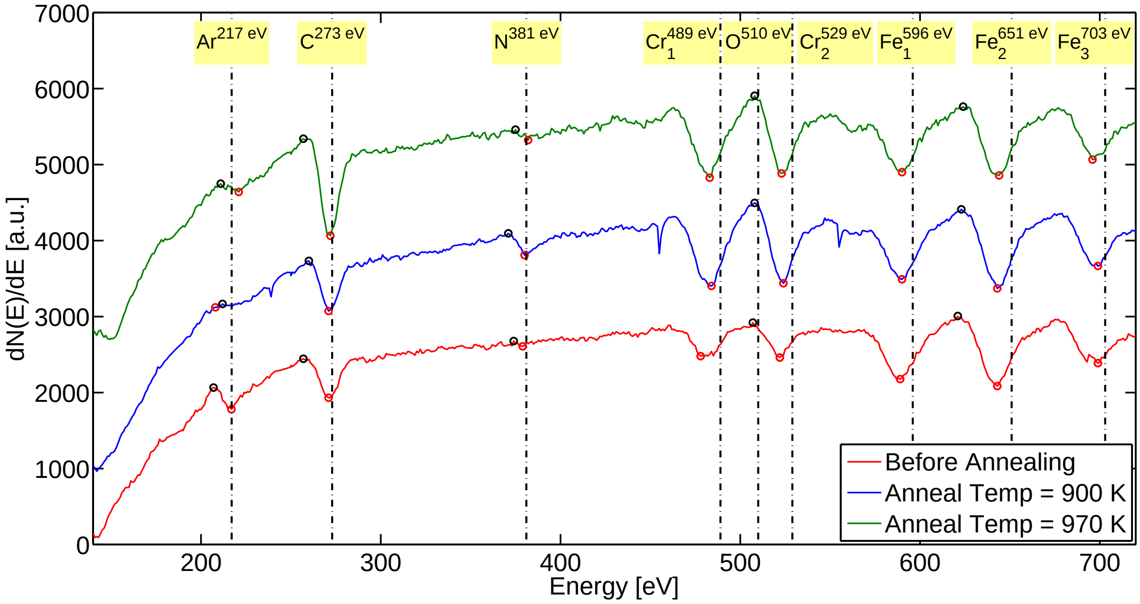

Figure 4.7: Three different AES spectra of ferritic stainless steel (100) surface: After sputtering and after two annealing temperatures of 900 K and 970 K. The dashed black lines mark the energy of the Auger electrons, which are obtained for different elements from an AES atlas. The black and red circles mark the intensities used for the peak to peak ratios to compare the concentration.

AES spectra, LEED patterns and IV-curves of the surface were obtained after the sputtering process, after the two different annealing processes and after the adsorption experiment for every used surface temperature and annealing temperature. There were no qualitative differences in the obtained data before and after the adsorption experiments, which only leaves the comparison between the sputtering process and the two annealing processes. The AES spectra after annealing showed a tremendous increase in Cr at the surface compared to the spectrum before annealing (Fig.4.7). This means the surface is Cr enriched and is binding either to C or N. For an annealing temperature of 900 K the surface shows a higher N

Table 4.1: Comparison of the peak to peak ratios of the cleaned surface after sputtering, after annealing with 900 K and after annealing with 970 K. For the ratio of Cr the Cr_2 peak and for the ratio of Fe the Fe_2 peak were taken (Fig.4.7).
r ... peak to peak ratio of an element.
T_A ... annealing temperature.

Preparation	$\frac{r_{Ar}}{r_{Fe}}$[a.u.]	$\frac{r_C}{r_{Fe}}$[a.u.]	$\frac{r_N}{r_{Fe}}$[a.u.]	$\frac{r_{Cr}}{r_{Fe}}$[a.u.]	$\frac{r_{Fe}}{r_{Fe}}$[a.u.]
cleaned	0.31	0.56	0.08	0.50	1.00
$T_A = 900\,\mathrm{K}$	0.04	0.63	0.28	1.02	1.00
$T_A = 970\,\mathrm{K}$	0.12	1.41	0.15	1.13	1.00

concentration than before the annealing process but still with a good amount of C. In this case Cr has the chance to bind to both C and to N. If the annealing temperature is further increased up to 970 K the N content decreases, which motivates the Cr to bind more to C atoms. The peak to peak intensity ratios for Ar, C, N, Cr and Fe peaks were used to give information on the change in the chemical composition of the surface, which can be compared to the work of C. Uebing et al [51]. The position of the O-peak was marked in the spectra because the oxidization, the bonding of H_2O or OH groups to Cr was expected though no peak was observed. But in the LEED pattern it will be shown that an oxidization process or the adsorption of water occurred. Since there were several peaks for Fe and Cr, the intensity ratios of the Cr_2 peak and the Fe_2 peak were taken. The results for the peak to peak ratios can be seen in table 4.1. The ratios in the table are normalized, which means the ratios from the figure are divided by the most stable peak to peak ratio Fe_2. In order to calculate the mole fraction according to equation 2.49 the sensitivity factor for every element would have been necessary, which wasn't obtained for this setup.

AES measurements proved to be difficult because the O-peak didn't show any change before and after water adsorption experiments. The main reason behind this is either the weak sensitivity for Auger electrons from the O peak or stimulated desorption of water molecules caused by electron beams [52]. One way to avoid this problem is to utilize stimulated desorption in a different way. A.E. Prodromides et al [53] showed that stimulated desorption of water leads to a change in the shape of

Auger spectra without the detection of the O-peak. In our case water would bind to Cr and therefore replaces C and N. It could be expected that the peaks of these elements experience a change but our AES data didn't show any. One explanation might be the following consideration. The annealing process itself (Fig.4.7) already caused the segregation of Cr and O to the surface. The stimulated adsorption then wouldn't change the AES data because the surface is already enriched with Cr and it would leave no obvious change in the chemical composition in the near surface region. One solution consists of skipping the annealing process. Then the Cr content at the surface is far lower and due to the segregation of Cr to the surface induced by water, the intensity of the Cr-peak will increase after the adsorption process though no oxygen can be seen by the AES. Another way is to proof the reduction of the oxidation rate by the formed OH-layers, which hinder the ion diffusion during the later stages of oxidation [4]. This is done by measuring AES after two conducted adsorption experiments. One experiment is the adsorption of O after cleaning the surface of the stainless steel sample and the other one is the adsorption of O on the stainless steel sample with a preadsorbed OH-layer. Comparing those two spectra the O peak should be smaller on the sample with the preadsorbed OH-layer, which proves its existence.

The structure that is induced by the annealing processes can be seen in the LEED pattern (Fig.4.8). The LEED pattern didn't show a qualitatively change upon adsorption experiments with water. Therefore, only the pattern with a surface temperature of 400 K during adsorption were taken as representation. The red circles mark the intensities of the (10) spots, the green circles mark, where the (11) spots will appear, when the energy of the electron beam is increased, and the blue circle marks the intensity of one spot of the overlay structure. The beam energy, when the pattern was recorded, can be seen on the lower left part of each figure. After the sputtering process a superlattice doesn't really exist though, there is a very weak blur indicating the spot positions. For an annealing temperature of 900 K a circular shape can be observed. This circle indicates the formation of the Cr-O or Cr-OH layers by the residual gas or by the segregation of O from the bulk of the sample, which will be discussed later. Further annealing to a temperature of 970 K also enriches the surface with C atoms and the solid circle molders into spots.

The positioning of this superlattice to the primitive (1×1) spots of the substrate (compare to fig.2.3 (a)) can be determined according to chapter 2.3.4. Figure 4.9 (a) describes the LEED pattern and includes the reciprocal lattice vectors of the substrate and the superlattice. It should be noticed that due to the symmetry of the substrate, the superlattice has two domains marked as blue and red spots and the intersection of both is marked as magenta. The reciprocal lattice vectors for the blue domain are: $b^*_{b1} = 2/5 * a^*_1 + 1/5a^*_2$ and $b^*_{b2} = -1/5 * a^*_1 + 2/5a^*_2$, whereas the vectors for the red domain are: $b^*_{r1} = -1/5 * a^*_1 - 2/5a^*_2$ and $b^*_{r2} = 2/5*a^*_1 - 1/5a^*_2$. By forming the matrix notation of the reciprocal vectors (Eq.2.40) and then transforming it to the real space lattice (Eq.2.45), the basis vectors can be determined, which are $b_{b1} = 2*a_1 + 1a_2$ and $b_{b2} = -1*a_1 + 2a_2$ for the blue domain and $b_{r1} = -1*a_1 - 2a_2$ and $b_{r2} = 2*a_1 - 1a_2$ for the red domain. The real space arrangement can be observed in figure 4.9 (b). In the work of H. Fujiyoshi et al [54] this supperlattice was described as the bonding between Cr and O. Furthermore, it can be excluded that this structure comes from the bonding of Cr to N or C because in the work of C. Uebing [55] Cr/N and Cr/C exhibit a (1x1) superstructure. Therefore, the observed structure is $Fe - 17Cr(100) - (\sqrt{5} \times \sqrt{5})R27° - O$ or a $Fe - 17Cr(100) - (\sqrt{5} \times \sqrt{5})R27° - OH$ after the annealing process because water forms OH-groups on the surface [4]. It can be assumed that either the AES apparatus isn't sensitive enough to detect Auger electrons for O or the electron beam stimulates the desorption of OH-groups [53].

The work of P. Jussila et al [4] showed that the adsorption of H_2O induce the segregation of Cr to the surface, which binds to the OH-layer. This motivates the assumption that O and OH exhibit the same supperlattice on Cr. This means that during the annealing process the surface has the chance to react with the residual gas, which consists of water and/or O. It should be noted that stainless steel rather react with O over water vapor [56]. One way to proof the assumption is by measuring TD spectra after the LEED measurement, since AES in general has problems to detect Auger electrons at the O-peak in this setup because the O-peak also overlaps with the Cr-peak. By comparing the signals from H_2O, OH and O, the amount of O and OH groups on the surface can be determined. The TD spectra though has to be analyzed critically because the electron beam of the

LEED experiment might cause additional reactions on the surface of the sample.

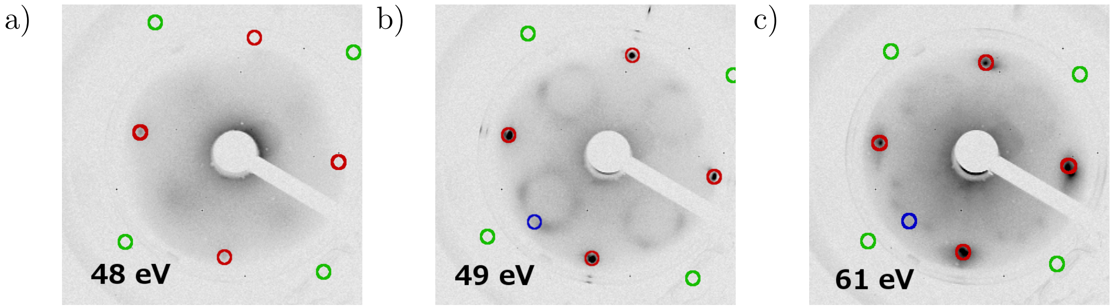

Figure 4.8: LEED patterns of Fe-17Cr (100) surface (a) after sputtering (b) after annealing at a temperature of 900 K and (c) after annealing at a temperature of 970 K. On both (b) and (c) adsorption experiments at a surface temperature of 400 K were conducted beforehand.

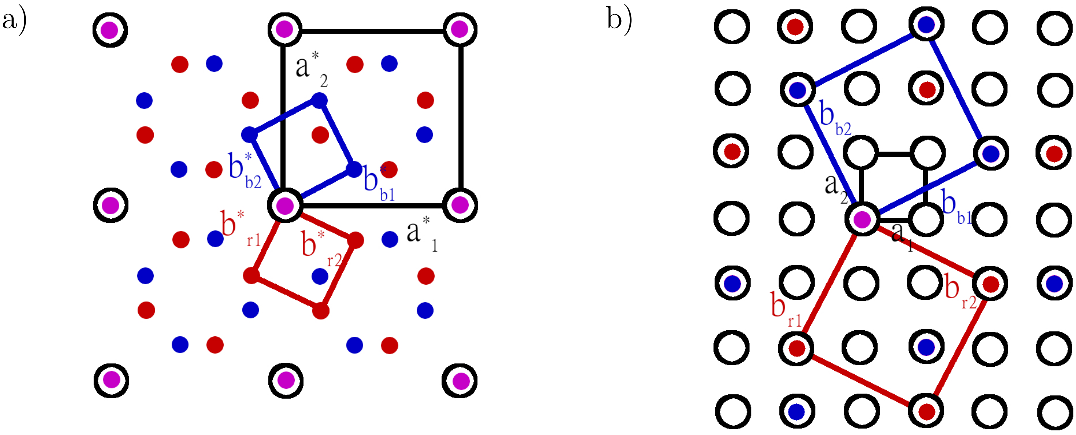

Figure 4.9: Analysis of the obtained LEED patterns showing the $(\sqrt{5} \times \sqrt{5})R27^\circ$ overlay structure in (a) schematics of the LEED pattern and (b) schematics in real space[57].

Moreover, the LEED patterns contained information of the atomic distance alongside the surface and into the bulk direction, which is described by the IV-curves. As for the atomic distance along the surface the energy was measured, when two (10) spots became visible on the edge of the LEED screen. From the measured energy it's possible to obtain the wavelength λ of the Ewald sphere (Eq.2.37). The LEED screen itself only measure a part of the Ewald sphere that is defined by the viewing angle of the LEED screen. In our case the angle was 90°. At a verti-

Table 4.2: Measured energies for different crystal patterns and calculated atomic distances for annealing temperatures of 900 K (left part of the table) and 970 K (right part of the table).
E ... measured energy, when two opposite lying spots occur in the LEED pattern.
a ... calculated atomic distance from the measured energy according to equations 2.37 and 2.47.

E_{900} $[eV]$	a_{900} $[\AA]$	E_{970} $[eV]$	a_{970} $[\AA]$
42	2.67	41	2.70
41	2.70	42	2.67
39	2.77	42	2.67
40	2.73	39	2.77
40	2.73	38	2.80
39	2.77	42	2.67
42	2.67	41	2.70
42	2.67	42	2.67
43	2.64	41	2.70
41	2.70	40	2.73
41	2.70	42	2.67
41	2.70	42	2.67
42	2.67	43	2.64
41	2.70	42	2.67
41	2.70	42	2.67
		40	2.73
		39	2.77
		42	2.67
		40	2.73

cal incident of the electron beam, the diffracted angle θ for one of our outermost points become 45°, which is half of the viewing angle [58, Fig. 1.14]. By utilizing equation 2.37 and 2.47, the atomic distance between two adjacent atoms, which in our case is equivalent to the lattice constant, can be calculated. The results for the two annealing temperatures can be seen in table 4.2 (The whole data involves obtained LEED patterns before and after adsorption experiments), which show that no real rearrangement along the surface took place because the atomic distance didn't really change. The average values for an annealing temperature of 900 K was $a = [2.70 \pm 0.04]$ Å and for 970 K $a = [2.70 \pm 0.04]$ Å. The single measurement directly after the sputtering process resulted in an atomic distance of $a = 2.61\,\text{Å}$. These results are very close to the bulk lattice constants of iron $a_{Fe} = 2.87\,\text{Å}$ and chromium $a_{Cr} = 2.88\,\text{Å}$ [59],[60, p.265-266].

The situation though is different in the local arrangement. From the IV-curves (Fig. 4.10) it can be seen that some rearrangement took place. The intensity of the (11) spots show an additional peak in the range of 100 - 120 eV for the peaks after annealing. For the intensity of the (10) spots the peaks at around 100 eV and 150 eV fuse together for an annealing temperature of 970 K. The distance between the peaks can be taken to evaluate the distance between the supperlatice to the bulk and the difference in intensity for the arrangement of the supperlatice to the underlying structure of the substrate. To be able to make exact predictions of these properties, further experiments with different annealing temperatures between the two used temperatures need to be conducted.

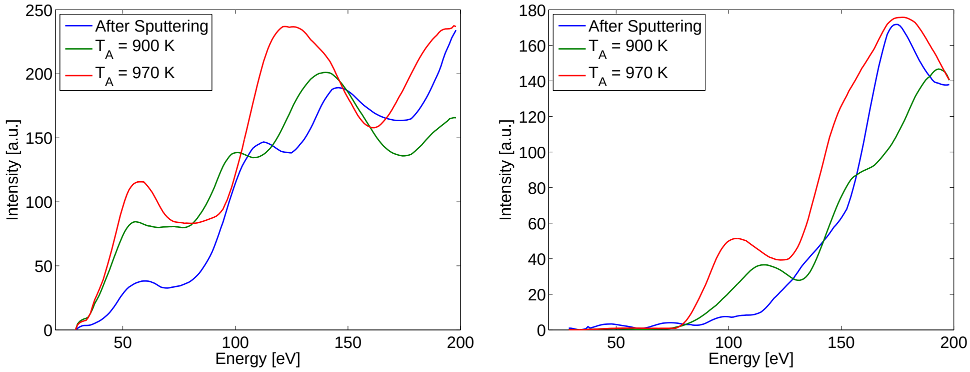

Figure 4.10: IV curves of the obtained LEED patterns after sputtering and after the two annealing temperatures of 900 K and 970 K. The IV curves can be distinguished into the average intensity of the four (10) spots [left side] and the four (11) spots [right side].

The fact that no difference was measured neither in the chemical nor in the crystal patterns before and after adsorption experiments for every used surface temperature, has the following main reason. The electrons used for investigation in LEED and AES experiments support the desorption of water molecules. This means that the adsorbed water is already desorbed when the data is recorded [42, p.383-384].

5 Summary

The adsorption of water on a Fe-17Cr(100) surface was investigated with MBSS, TDS, LEED and AES. Before every adsorption experiment the Fe-17Cr sample was cleaned by Ar-ion sputtering for 10 minutes and annealed at two different temperatures of 900 K and 970 K with a duration of 10 minutes each. The change in the surface properties by the annealing process was observed with LEED and AES. The measurements showed the removal of the Ar-content, which resulted from the Ar-ion sputtering, and two increased Cr peaks. Since a superstructure was observed that matches an oxidized surface, the increased Cr peaks are a combination of Cr segregation from the bulk and an enrichment of O on the surface because the Cr and O peaks are overlapping. The O enrichment resulted either from the segregation of O from the bulk or the adsorption of residual gas, which consisted mainly of water and O_2 molecules. Therefore, the built superstructure can be identified as Fe-17Cr-$(\sqrt{5}x\sqrt{5})R27°$-O/OH, which is a combination of O and H_2O coadsorption, whereas the adsorption of water most likely underwent a dissociation process due to the high surface temperatures during the annealing process. The difference between the two annealing temperatures consisted in an increased N content for an annealing temperature of 900 K and an increased C content for an annealing temperature of 970 K. The enrichment of N and C resulted from a combination of segregation and the adsorption of residual gas.

In order to investigate the adsorption of water molecules, the MBSS system was enhanced by attaching a glass reservoir filled with deionized water and applying heating tapes to the reservoir and the pipelines for evaporating the water as well as preventing condensation inside the pipelines. The nozzle of the MBSS system was kept at the constant temperature of 700 K for the experiments. The water beam was seeded with He to gain higher kinetic energies. The characterization of the water beam was done by TOF experiments to determine the translational energy, the terminal temperature and the percentage of water in the seeded beam. The determination of the beam flux was done by an indirect method. An adsorption experiment at very low sample surface temperatures was conducted. The time for the formation of one water monolayer was measured, which leads to the beam flux. Therefore, the properties of the beam are the translational energy $E_t = [248 \pm 17]\,\text{meV}$, the terminal temperature $T_{term} = [429 \pm 26]\,\text{K}$, the flux $F = 7.73 * 10^{13}\,\text{molecules/cm}^2\text{s}$ and $[24 \pm 8\,]\%$ of water in the He/water gas mixture.

The adsorption experiments based on "The direct reflectivity method of King and Wells" were conducted for the surface temperatures of 323 K and 400 K. The 4 obtained initial sticking coefficients were very similar and ranged from 0.24 to 0.35 with an average of $S_0 = 0.32$. Furthermore, the sticking coefficient was constant at the beginning of the adsorption experiment revealing a precursor-mediated adsorption process. TDS experiments were conducted for the surface temperatures of 150 K and 323 K during adsorption. The experiment for 150 K showed two desorption peaks with the desorption energies $E_{d,1} = 0.59\,\text{eV}$ for the first peak at the desorption temperature $T_1 = 223\,\text{K}$ and $E_{d,2} = 1.38\,\text{eV}$ for the second peak at the desorption temperature $T_2 = 511\,\text{K}$. These two peaks were identified as first order peaks due to the very low surface temperature. For the desorption experiments at the surface temperature of 323 K during adsorption no peaks were observed, which would indicate dissociation processes for water during the annealing. AES and LEED experiments didn't show a qualitative change upon adsorption, indicating that during the annealing procedure most of the possible adsorption sites for water were occupied with O and OH.

Bibliography

[1] P. Marcus. *Thin Oxide Film Formation on Metals.* Corrosion Technology. CRC Press, 2002.

[2] M. A. Henderson. The interaction of water with solid surfaces: fundamental aspects revisited. *Surface Science Reports*, (46):1–308, 2002.

[3] D. A. Harrington, A. Wieckowski, S. D. Rosasco, B. C. Schardt, G. N. Salaita, A. T. Hubbard, and J. B. Lumsden. Films formed on well-defined stainless steel single-crystal surfaces in oxygen and water: studies of the (111) plane by LEED, Auger and XPS. *Corrosion Science*, 25(10):849–869, 1985.

[4] P. Jussila, H. Ali-Löytty, K. Lahtonen, M. Hirsimäki, and M. Valden. Inhibition of initial surface oxidation by strongly bound hydroxyl species and Cr segregation: H_2O and O_2 adsorption on Fe–17Cr. *Surface Science*, 603(19):3005–3010, 2009.

[5] M. Lampimäki, K. Lahtonen, P. Jussila, M. Hirsimäki, and M. Valden. Morphology and composition of nanoscale surface oxides on Fe–20Cr–18Ni(111) austenitic stainless steel. *Journal of Electron Spectroscopy and Related Phenomena*, 154(3):69–78, 2007.

[6] H. Ali-Löytty, P. Jussila, M. Hirsimäki, and M. Valden. Influence of CrN surface compound on the initial stages of high temperature oxidation of ferritic stainless steel. *Applied Surface Science*, 257(17):7783–7791, 2011.

[7] H. Ali-Löytty, P. Jussila, T. Juuti, L. Karjalainen, A. Zakharov, and M. Valden. Influence of precipitation on initial high-temperature oxidation of

Ti–Nb stabilized ferritic stainless steel SOFC interconnect alloy. *International Journal of Hydrogen Energy*, 37(19):14528–14535, 2012.

[8] G. E. Totten. *Steel Heat Treatment: Metallurgy and Technologies.* Steel Heat Treatment Handbook, Second Edition. Taylor & Francis, 2006.

[9] R. Jones, editor. *Environmental Effects on Engineered Materials.* Corrosion Technology. CRC Press, 2001.

[10] W. Soboyejo. *Mechanical Properties of Engineered Materials.* CRC Press, 2002.

[11] K. W. Kolasinski. *Surface Science : Foundations of Catalysis and Nanoscience.* John Wiley & Sons, third edition, 2012.

[12] M. R. Lynden-Bel, S. C. Morris, J. D. Barrow, J. L. Finney, and L. Charles. *Water and Life.* CRC Press, 2010.

[13] S. J. Grabowski, editor. *Hydrogen Bonding—New Insights.* Springer Netherlands, 2006.

[14] H.-J. Freund and H. Knözinger. Foreword for the Gerhard Ertl Festschrift. *The Journal of Physical Chemistry B*, 108(38):14183–14186, 2004.

[15] H. J. Butt, K. Graf, and M. Kappl. *Physics and Chemistry of Interfaces.* John Wiley & Sons, 2006.

[16] P. Junell. *Molecular Beam Surface Scattering Studies of CO and* O_2 *Adsorption Processes on Clean and Modified Pd[110] and Cu[100] Surfaces.* PhD thesis, Tampere University of Technology, 2004.

[17] S. Larsson. *Chemical Physics.* CRC Press, 2012.

[18] K. Oura, V.G. Lifshits, A. A. Saranin, A. V. Zotov, and M. Katayama. *Surface Science: An Introduction.* Advanced Texts in Physics. Springer, 2003.

[19] J. H. Larsen and I. Chorkendorff. From fundamental studies of reactivity on single crystals to the design of catalysts. *Surface Science Reports*, 35(5-8):163–222, 1999.

[20] I. Chorkendorff. *The XPS and AES Methods for Surface Analysis in Material Science*. Technical University of Denmark. Physics, 1994.

[21] D. A. King and M. G. Wells. Molecular beam investigation of adsorption kinetics on bulk metal targets: nitrogen on tungsten. *Surf. Sci*, (29):454–482, 1972.

[22] G. Scoles, D. Bassi, and U. Buck. *Atomic and Molecular Beam Methods*. Oxford University Press, USA, 1988.

[23] J. Libuda and H.-J. Freund. Molecular beam experiments on model catalysts. *Surface Science Reports*, 57(7-8):157–298, 2005.

[24] M. Fárník. *Molecular Dynamics in Free Clusters and Nanoparticles*. PhD thesis, VŠCHT Praha, 2011.

[25] G. D. Stein. Cluster beam sources: Predictions and limitations of the nucleation theory. *Surface Science*, 156:44–56, 1985.

[26] O. F. Hagena. Nucleation and growth of clusters in expanding nozzle flows. *Surface Science*, 106(1-3):101–116, 1981.

[27] C. Bobbert, S. Schütte, C. Steinbach, and U. Buck. Fragmentation and reliable size distributions of large ammonia and water clusters. *The European Physical Journal D*, 19(2):183–192, 2002.

[28] U. Buck and F. Huisken. Infrared spectroscopy of size-selected water and methanol clusters. *Chemical reviews*, (100):3863–3890, 2000.

[29] G. A. Somorjai and Y. Li. *Introduction to Surface Chemistry and Catalysis*. John Wiley & Sons, 2010.

[30] H. Lüth. *Surfaces and interfaces of solids*. Springer series in surface sciences. Springer-Verlag, 1993.

[31] C. Weissmantel and C. Hamann. *Grundlagen der Festkörperphysik*. Hochschulbücher für Physik. Barth, 1995.

[32] Y. Huang. *Adsorption of Chiral Molecules on Naturally Chiral Surfaces and Chirally Templated Surfaces.* PhD thesis, Carnegie Mellon University, 2008.

[33] J. Rivière and S. Myhra, editors. *Handbook of Surface and Interface Analysis.* CRC Press, 2009.

[34] P. Marcus and F. Mansfeld, editors. *Analytical Methods in Corrosion Science and Engineering.* Corrosion Technology. CRC Press, 2005.

[35] J. Cazes, editor. *Analytical Instrumentation Handbook, Third Edition.* CRC Press, 2004.

[36] G. Svehla. *Ultraviolet Photoelectron and Photoion Spectroscopy, Auger Electron Spectroscopy, Plasma Excitation in Spectrochemical Analysis.* Comprehensive Analytical Chemistry. Elsevier Science, 1979.

[37] K. Andersson, A. Gómez, C. Glover, D. Nordlund, H. Öström, T. Schiros, O. Takahashi, H. Ogasawara, L. Pettersson, and A. Nilsson. Molecularly intact and dissociative adsorption of water on clean Cu(110): A comparison with the water/Ru(001) system. *Surface Science*, 585(3):L183–L189, 2005.

[38] T. Kondo, D. Mori, R. Okada, and S. Yamamoto. Molecular Beam Study of H_2O Interaction with Pt(111). *Japanese Journal of Applied Physics*, 43(3):1104–1109, 2004.

[39] M. Ahonen. *Adsorption Dynamics Studies on the Nanoscale Oxidation of Clean and Structurally Modified Cu(100) Surface.* PhD thesis, Tampere University of Technology, 2008.

[40] J. Pere. *Time-of-flight analysis of supersonic molecular beams for surface reactions dynamics studies.* Licentiate thesis, Tampere University of Technology, 1999.

[41] U. Buck and R. Krohne. Cluster size determination from diffractive He atom scattering. *The Journal of Chemical Physics*, 105(13):5408, 1996.

[42] A. Hodgson and S. Haq. Water adsorption and the wetting of metal surfaces. *Surface Science Reports*, 64(9):381–451, 2009.

[43] D. Brinkley, M. Dietrich, T. Engel, P. Farrall, G. Gantner, A. Schafer, and A. Szuchmacher. A modulated molecular beam study of the extent of H_2O dissociation on $TiO_2(110)$. *Surface Science*, 395(2-3):292–306, 1998.

[44] P. Miranda, L. Xu, Y. Shen, and M. Salmeron. Icelike Water Monolayer Adsorbed on Mica at Room Temperature. *Physical Review Letters*, 81(26):5876–5879, 1998.

[45] A. Lorek. *Flüssiges unterkühltes Grenzflächenwasser in der Marsoberfläche.* PhD thesis, Potsdam, 2008.

[46] D. R. Lide. *CRC Handbook of Chemistry and Physics: A Ready-reference Book of Chemical and Physical Data.* CRC Handbook of Chemistry and Physics, 85th Ed. CRC Press, 2004.

[47] J. Libuda, I. Meusel, J. Hartmann, and H.-J. Freund. A molecular beam/surface spectroscopy apparatus for the study of reactions on complex model catalysts. *Review of Scientific Instruments*, 71(12):4395, 2000.

[48] M. Laurin, V. Johánek, A. W. Grant, B. Kasemo, J. Libuda, and H.-J. Freund. Local reaction rates and surface diffusion on nanolithographically prepared model catalysts: experiments and simulations. *The Journal of Chemical Physics*, 122(8):84713, 2005.

[49] J. P. Joly, F. Gaillard, E. Peillex, and M. Romand. Temperature-programmed desorption (TPD) of water from iron, chromium, nickel and 304L stainless steel. *Vacuum*, 59(4):854–867, 2000.

[50] E. Murray, J. Prasad, H. Cabibil, and J. Kelber. The interaction of H_2O and Cl_2 on Fe polycrystalline surfaces. *Surface Science*, 319(1-2):1–9, 1994.

[51] C. Uebing, V. Scheuch, M. Kiskinova, and H. P. Bonzel. Segregation of ordered CrN and CrC surface phases on a Fe-15Cr(100) crystal. *Surface Science*, 321(1–2):89–99, 1994.

[52] S. Patel and M. Pemble. Auger electron spectroscopic (AES) studies of the adsorption and reaction of $SnCl_4$ and H_2O at a silica surface. *Surface Science*, 352-354(95):534–539, 1996.

[53] A. E. Prodromides, C. Scheuerlein, and M. Taborelli. The characterisation of non-evaporable getters by Auger electron spectroscopy: analytical potential and artefacts. *Applied Surface Science*, 191(1-4):300–312, 2002.

[54] H. Fujiyoshi, T. Matsui, and J. Yuhara. Segregation and morphology on the surface of ferritic stainless steel (001). *Applied Surface Science*, 258(19):7664–7667, 2012.

[55] C. Uebing. Formation of Surface Compunds on Fe-15Cr(100) Single Crystals. *Surface Science*, 225:97–106, 1990.

[56] C. Palacio, H. Mathieu, V. Stambouli, and D. Landolt. XPS study of in-situ oxidation of an Fe-Cr alloy by low pressure oxygen in the presence of water vapor. *Surface Science*, 295(1-2):251–262, 1993.

[57] F. Rammer, K. Hermann, and M. A. V. Hove. LEEDpat Version 1.0.

[58] B. Bhushan. *Handbook of Micro/Nano Tribology, Second Edition.* CRC Press, 1998.

[59] L. Zwell, D. E. Carnahan, and G. R. Speich. Lattice parameter of ferritic and martensitic Fe-Ni alloys. *Metallurgical Transactions*, 1(4):1007–1009, 1970.

[60] K. Hermann. *Crystallography and Surface Structure.* Wiley-VCH Verlag GmbH & Co. KGaA, Weinheim, Germany, 2011.